# Finite Element Modeling of Indentation Tests and Neural Network Model Applications

## Modelování indentačních testů metodou konečných prvků a aplikace modelu neuronových sítí

Diploma Thesis

Student: Bc. Phu Ma Quoc

Personal number: maq0005

Supervisor: Sebastián Basterrech, Ph.D.

Ostrava 2022/2023

# Diploma Thesis Assignment

Student:                    **Bc. Phu Ma Quoc**

Study Programme:            N0715A270033 Applied Mechanics

Title:            Finite Element Modeling of Indentation Tests and Neural Networks
Model Applications
Modelování indentačních testů metodou konečných prvků a aplikace
modelu neuronových sítí

The thesis language:                    English

Description:

Description:
1) State of the art related to usage of indentation tests for material parameters calibration.
2) Experiments realization for SS304.
3) Calibration of appropriate material model(s).
4) Design of indentation experiments.
5) Finite element model creation.
5) Modeling applying Neural Networks.
6) Conclusions.

References:

1. J.F. Doyle, Modern Experimental Stress Analysis: completing the solution of partially specified
problems, Wiley & Sons, UK, 2004.
2. Juergen Schmidhuber, Deep Learning in Neural Networks: An Overview, Neural Networks, Vol. 61,
pages 85-117, 2015.
3. Yoshua Bengio, Deep Learning of Representations: Looking Forward, Department of Computer Science
and Operations Research, University of Montreal, Canada, 2013. Available at: http://goo.gl/OK0WV9 .
4. Hastie, T., Tibshirani, R., Friedman, J., The Elements of Statistical Learning: Data Mining, Inference,
and Prediction. Second Edition, Springer, February 2009.

Extent and terms of a thesis are specified in directions for its elaboration that are opened to the public on
the web sites of the faculty.

Supervisor:                    **Sebastian Basterrech, PhD.**

Date of issue:            15.12.2022

Date of submission:        12.05.2023

Study programme guarantor: doc. Ing. Martin Fusek, Ph.D.

In IS EDISON assigned: 15.12.2022 14:27:04

# Abstract

Instrumented Indentation Test (IIT) has been developed in the last decades to be one of the most versatile and convenient tests for the mechanical properties of metallic materials. In IIT, simply by following the procedure of conventional hardness measurement, it is possible to obtain from the material not only the hardness but also the tensile data, parameters for its plasticity model, fracture toughness, and weld residual stress. The method can be conducted on a considerably small scale. Therefore, it can measure components in situ without the need to isolate them from their working condition or to machine samples from equivalent materials for tensile tests. The IIT based on the traditional approach (stress-strain approach) requires a complicated machine setup to accurately measure the area of the imprint under the indenter; the reaction force the specimen exerts on the indenter, and the depth of the indenter head to plot their relation, yielding a Force-Depth (F-D) curve. These results are essential for evaluating the aforementioned mechanical properties of the material. Following this approach requires extensive knowledge of material sciences to derive analytical formulas for different material classes after several empirical studies. The method is, therefore, expensive as one attempt to study different classes of materials. Besides, for a soft material such as SS304L, which inherits an excessive pile-up/sink-in effect, the improperly measured imprint area poses another challenge for IIT.

This thesis attempts to solve the two inherent drawbacks of IIT by applying a Neural Network (NN) to capture a wider range of material property variation and replace the intricate analytical calculations. With this approach, Finite Element Method (FEM) is first employed to simulate IIT, from which several F-D curves can be simulated by varying parameters of the constitutive material model used for FEM. After a set of F-D curves is generated, it is used to train a Feed-Forward Neural Network (FFNN) so that when an arbitrary F-D curve is fed into the NN, it will output the corresponding parameters for the constitutive model of the material. The thesis aims to establish a workflow for such a process by attempting to create a NN with high accuracy to assist or replace the complicated analytical evaluation of IIT and the costly physical measurements. It is proven that this approach is feasible and the challenges are discussed during the whole thesis. Based on this, suggestions for future works are made to improve the performance of the NN approach.

*Keywords:* Instrumented Indentation Testing, Finite Element Method, Neural Network, Feed-Forward Neural Network, SS304L, tensile properties

# Acknowledgement

# Anotace

Bc. Phu Ma Quoc *Topic in Czech: diplomová práce.* Ostrava: VŠB - Technická univerzita Ostrava, Fakulta strojní, Katedra aplikované mechaniky, 2022, xx stran. Vedoucí práce: Sebastián Basterrech, Ph.D.

Diplomová práce zkoumá modelování instrumentovaného indentačního testu (IIT) s využitím metody konečných prvků (MKP) a neuronových sítí (NN). Cílem práce je vytvořit NN, která bude schopna vyhodnotit experimentální data z realizovaného IIT takovým způsobem, aby přímo kalibrovala vhodný model plasticity. Studie je prováděna na austenitické nerezové oceli SS304L, která představuje výzvu pro IIT. K dosažení cíle je proveden IIT na vzorku SS304L k získání závislosti hloubky zatlačení na reakční síle, kterou materiál vyvíjí na vtlačovanou kuličku. Kromě toho jsou na stejném materiálu provedeny tahové zkoušky s digitální korelací obrazu (DIC) k získání tahové deformační křivky, z které lze identifikovat parametry konstitutivního modelu. Výsledky z IIT a tahové zkoušky jsou poté použity k vytvoření MKP modelu. S využitím FEM modelu lze simulovat několik IIT a vytvořit tak soubor dat pro trénování NN v rozsahu austenitických ocelí. Tento soubor dat je vložen do NN. K nalezení optimální architektury pro dosažení finálního cíle jsou provedeny numerické experimenty. Práce navrhuje rámec a dokazuje jeho proveditelnost při uvažování Armstrong-Frederickova modelu zpevnění se třemi parametry. Všechna data a zjištěné výzvy jsou zaznamenány a diskutovány.

# Annotation

Bc. Phu Ma Quoc *Study of Topological Optimization: Master Thesis.* Ostrava: VŠB - Technical University of Ostrava, Faculty of Mechanical Engineering, Department of Applied Mechanics, 2022, xx pages. Supervisor: Sebastián Basterrech, Ph.D.

The diploma work investigates the Instrumented Indentation Test (IIT) modelling with Finite Element Method (FEM) and Neural Network (NN). The final goal is to create a NN that can evaluate the experimental data from a physical IIT in such a way to directly calibrate a suitable plasticity model. The study is conducted on an austenitic stainless steel SS304L which is a challenge for IIT. To achieve the goal, IIT is performed on a SS304L specimen to obtain the indenting depth versus the reaction force the material exerts on the indentation ball. Besides, tensile tests with Digital Image Correlation (DIC) on the same material are performed to obtain the tensile stress-strain curve, from which parameters of a constitutive model can be identified. The results from IIT and tensile test are then used to establish a FEM model. Using the FEM model, several IITs can be simulated to create a dataset for NN training in the range of austenitic steels. This dataset is fed into a NN and numerical experiments are done to find an optimal architecture for the final goal. The thesis proposes a framework and proves its feasibility considering Armstrong-Frederick hardening model with three parameters. All the data and identified challenges are reported and discussed.

# Contents

# List of Symbols

| Symbol | Definition | Unit |
|---|---|---|
| $A$ | Cross-sectional area of the tensile specimen | [mm$^2$] |
| $L$ | Instantaneous length of the tensile specimen | [mm] |
| $L_0$ | Original length of the tensile specimen | [mm] |
| $E$ | Young's modulus | [MPa] |
| $\nu$ | Poisson's ratio | [ - ] |
| $\sigma$ | Stress | [MPa] |
| $\sigma_{true}$ | True stress | [MPa] |
| $\sigma_y$ | Yield stress/strength | [MPa] |
| $\sigma_{eq}$ | Equivalent (von Mises) stress | [MPa] |
| $\sigma_u$ | Ultimate stress/strength | [MPa] |
| $\varepsilon$ | Strain | [ - ] |
| $\varepsilon_{trans}$ | Strain in transversal direction | [ - ] |
| $\varepsilon_{axial}$ | Strain in axial/longitudinal direction | [ - ] |
| $\varepsilon_{true}$ | True strain | [ - ] |
| $\varepsilon_{pl}$ | Plastic strain | [ - ] |
| $\varepsilon_{pl,true}$ | True plastic strain | [ - ] |
| $\dot{\varepsilon_{pl}}$ | Accumulated (equivalent) plastic strain rate | [%/s] |
| $\sigma_\infty$ | Material parameter (Armstrong-Frederick model) | [MPa] |
| $C, C_i$ | Material parameter (Armstrong-Frederick model), $i$-th material parameter (Chaboche model) | [MPa] |
| $\gamma, \gamma_i$ | Material parameter (Armstrong-Frederick model), $i$-th material parameter (Chaboche model) | [ - ] |

| Symbol | Definition | Unit |
|--------|-----------|------|
| Sa | Areal average roughness | [$\mu$m] |
| $\gamma_v$ | Viscosity parameter (Perzyna model) | [ - ] |
| $m$ | Rate sensitivity parameter (Perzyna model) | [ - ] |
| $b_0$, $b_1$, $b_2$, $b_3$, $b_4$ | Variables instead of material parameters for Least Square Method fitting | [ - ] |
| $\varepsilon_{pl,1}$, $\varepsilon_{pl,10}$, $\varepsilon_{pl,100}$ | Plastic strain for tensile testing speed of 1 mm/min, 10 mm/min, 100 mm/min | [ - ] |
| $\dot{\varepsilon}_{pl,1}$, $\dot{\varepsilon}_{pl,10}$, $\dot{\varepsilon}_{pl,100}$ | Plastic strain rate for tensile testing speed of 1 mm/min, 10 mm/min, 100 mm/min | [%/s] |
| $\sigma_{\varepsilon_1\%}$ | Engineering stress at 1% engineering strain | [MPa] |
| $\varepsilon_{pl_1\%}$ | Plastic strain at 1% engineering strain | [ - ] |
| $\sigma_{CHAB,\varepsilon_1\%}$ | True stress calculated at 1% engineering strain using Chaboche model | [MPa] |
| $\sigma_{vp,1}$, $\sigma_{vp,10}$, $\sigma_{vp,100}$ | Visco-plastic stress calculated for tensile testing speed of 1 mm/min, 10 mm/min, 100 mm/min | [MPa] |
| $\sigma_{total,1}$, $\sigma_{total,10}$, $\sigma_{total,100}$ | Total true stress, summation of plastic true stress and visco-plastic stress for tensile testing speed of 1 mm/min, 10 mm/min, 100 mm/min | [MPa] |
| $x_i$ | $i$-th input of Neural Network | [ - ] |
| $w_i$ | $i$-th weight of Neural Network | [ - ] |
| $b$ | Bias of Neural Network | [ - ] |
| $\varphi()$ | Activation function of Neural Network | [ - ] |
| $y$ | Output of Neural Network | |

# List of Abbreviations

| Abbreviation | Definition |
| --- | --- |
| HB/HV/HR | Brinell/Vickers/Rockwell hardness |
| IIT | Instrumented Indentation Test |
| DSI | Depth-Sensing Indentation |
| AF | Armstrong-Frederick |
| CHAB | Chaboche |
| GAM | Generalized Additive Model |
| DIC | Digital Image Correlation |
| NDT | Non-Destructive Test |
| FoV | Field of View |
| FEM | Finite Element Method |
| PDE | Partial Differential Equations |
| VMS | Von-Mises Stress |
| LSM | Least Square Method |
| ML | Machine Learning |
| AI | Artificial Intelligent |
| NN | Neural Network |
| ReLU | Rectifier Linear Unit |
| ELU | Exponential Linear Unit |
| FFNN | Feed-Forward Neural Network |
| RNN | Recurrent Neural Network |
| F-D | Force-Depth |
| MSE | Mean Square Error, equivalent to LSM |

# List of Figures

# List of Tables

# Chapter 1

# Introduction

The traditional approach to determine tensile properties of a material from Instrumented Indentation Test (IIT) is called the stress-strain approach as described in [1]. It should be noted that this approach is applicable only for IIT with a metallic material using a spherical indenter. The test is divided into multiple subsequent loading-unloading cycles. From this, it is possible to record the relationship between the indenting force (F) and the depth (D) of the indentation ball as it penetrates through the tested specimen. This Force-Depth (F-D) curve is the backbone of the calculation of tensile properties that the following four steps.

Step 1: Determine the real contact area between the indentation ball and the tested material, taking into account the pile-up/sink-in effect.

Step 2: Calculate the true stress (from force and contact area) and true strain (from contact angle).

Step 3: Fit the true stress-true strain in Step 2 to a constitutive equation.

Step 4: Evaluate the tensile properties: Young's modulus (from the contact stiffness), yield strength (intercept of the plastic curve and elastic line), and tensile strength (with the concept of instability in tension).

Following this process, the tensile properties of a material from a F-D curve are obtained. However, the drawback of this approach is the need to employ a number of formulas while proceeding from one step to another. The formulas contain parameters that can be obtained only from multiple experiments, which inevitably narrows down the number of materials that can be tested and requires extensive knowledge of materials. The material used for the study is austenitic stainless steel SS304L, which has been a challenge for the evaluation of IIT because it is a soft material with extensive pile-up/sink-in effect.

To avoid lengthy, costly calculations and physical tests, this thesis investigates instead the Neural Network (NN) approach. The aim of this approach is to model the IIT with high accuracy using a NN model. The desired output is to build a NN that can evaluate the experimental data from a physical IIT to directly calibrate a suitable plasticity model. The workflow of the study is depicted in Figure 1.1.

The main components of the study are illustrated in Figure 1.1. First, tensile tests with Digital Image Correlation (DIC) are carried out on the SS304L tensile specimens to measure the stress-strain curve from which the true stress-true plastic strain is calculated. Then, a material model (constitutive model) is fitted to the true stress-true plastic strain curve using the Least Square Method (LSM).
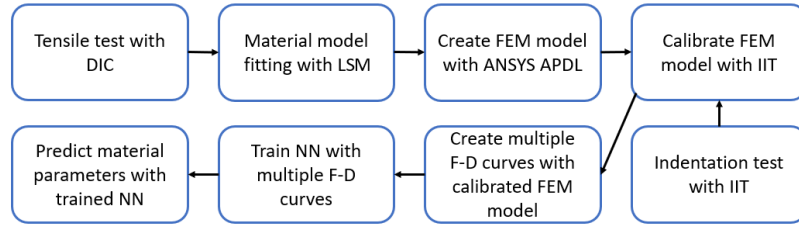
Figure 1.1: The workflow of the proposed approach.

The fitted material model is used to describe the plastic behavior of the material in a Finite Element Method (FEM) model, where IIT is simulated. The FEM model is constructed so that it can produce a highly accurate result within a relatively short time so that it is possible to automate the process for the generation of multiple F-D curves later. Specifically, an IIT simulation with FEM is a F-D curve, which is then calibrated with the F-D curve from the physical IIT. After calibration, the parameters of the material model are varied within given ranges to create multiple combinations of material parameters (configurations). These configurations are fed into the calibrated FEM model to create multiple F-D curves. Each configuration gives a different F-D curve, which helps us to substitute multiple lengthy and costly physical IITs.

Multiple F-D curves simulated from the previous step are then used for NN training. These data need to be standardized to facilitate easier training tasks. To find the optimal NN model for the task, there is a need to experiment with different structures, activation functions, etc. The loss value over epochs and the errors between the training data and the predicted data are the two key indicators for the evaluation of the NN performance. As a result, the thesis aims to obtain a well-trained NN that can take in a F-D curve and predict corresponding material parameters.

This thesis is organized as follows. Chapter 2 reviews the backgrounds of all the physical and numerical means used in this study. Chapter 3 reports the results from surface roughness measurement, IITs and tensile tests with DIC. Chapter 4 investigates the calibration of the strain-hardening and time-hardening material models with results from the tensile tests; simulation of the IIT in ANSYS APDL using different material models; and FEM model validation. Chapter 5 discusses the architecture of the NN chosen for the study and its implementation. Finally, the thesis is concluded and future works are discussed in Chapter 6.

# Chapter 2

# State of the Art

## 2.1   Instrumented Indentation Test

Hardness, by definition, is the resistance of a body against penetration of another body [2]. The higher the hardness of a body, the less the body is penetrated (deformed) under the load applied by another in contact with it. This phenomenon can be easily observed in real life as how easy ones feel as they use scissors to cut a pizza base in comparison with sheet metal. The historical scratch hardness scale introduced by Friedrich Mohs in 1822 has brought a good sense of hardness comparison to the scientific community and has been widely adopted in the mineralogy study and grinding tool assessment. The Mohs scale can be seen in Table 2.1.

Table 2.1: Mohs hardness scale based on ten different minerals.

| Mineral | Scale | Mineral | Scale |
|---------|-------|---------|-------|
| Talc | 1 | Orthoclase | 6 |
| Gypsum | 2 | Quartz | 7 |
| Calcite | 3 | Topaz | 8 |
| Fluorite | 4 | Corundum | 9 |
| Apatite | 5 | Diamond | 10 |

The scale is established based on the fact that any mineral that can scratch the other has higher hardness. According to the Mohs hardness scale, Talc has the lowest hardness while Diamond has the highest hardness. Most of the metal alloys used in engineering applications lie in the range of 4 to 9 Mohs hardness. Remarkably, the Mohs scale is limited only to metallic materials [2]. The scratch test is the oldest hardness test and has been developed ever since its first introduction with Mohs scale [3]. Interestingly, the relation between the hardness of the mineral with Mohs hardness of one and another with Mohs hardness of two is not linear as can be observed in Figure 2.1.

Instead of scratching, another branch of the hardness test focus on indenting a hard material (usually made of carbide or diamond) to a softer material to evaluate the hardness. For example, the Herbert pendulum hardness test introduced in 1923 employs a frame that swings on the tip of an indenter in direct contact with the testing specimen [5]. The rolling resistance can then be measured, from which the Herbert hardness is calculated [6]. However,
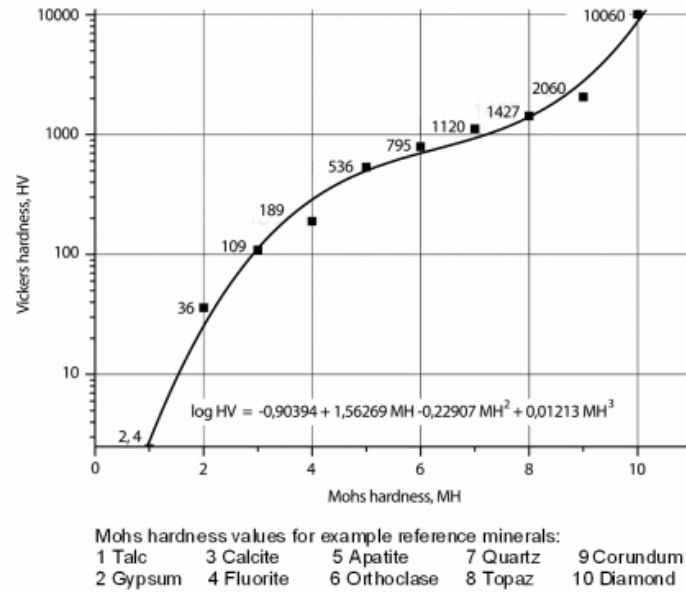
Figure 2.1: Nonlinearity of Mohs hardness with regard to Vickers hardness [4].

the method is not as widespread and well-standardized as other indentation methods such as Brinell (ISO 6506), Vickers (ISO 6507), and Rockwell (ISO 6509). These methods have the indenter pushed in the normal direction and in direct contact with the testing material. The deformed shape (imprint) of the indenter or its depth is evaluated to quantify the hardness. The three methods differ from one another depending on the geometry of the indenter, the load applications, the characteristic of the materials to be tested (soft or hard, thick or thin, the procedure to implement the force, measurement and calculation to obtain the numeric hardness values, etc.) The principle differences of the three hardness measuring methods are discussed in [2].

Specifically, Brinell method operates with the largest loads (up to 3000 kgf). Therefore, it can be used to measure thick specimens with rough surfaces (forging and casting). The indenter is spherical and made of tungsten carbide. On the other end, Vickers method works with the smallest range of loads (0.001 kgf to 120 kgf) and is primarily deployed for microhardness with loads below 1 kgf to characterize the microstructural phase hardness, case-hardened depths, dimensions of heat-affected zones in welding, etc. Thus, the surface preparation for this method is the strictest among the three methods. The indenter is pyramid-shaped and made of diamond. Finally, the Rockwell method allows different combinations of indenter types, sizes and loads. It is frequently used for testing sheet metal specimens with smooth surfaces. As opposed to the other two methods, where the hardness is defined by the area of the deformed area under the indenter, Rockwell hardness is calculated from the indentation depth.

The three methods are well-developed, so they have become relatively affordable and can provide highly accurate results in industrial applications. Additionally, the units used for hardness measurements such as Brinell hardness (HB), Vickers hardness (HV), and Rockwell hardness (HR), are not units but they represent measurement procedures from which the

hardness values are obtained. This means that they cannot be put under conventional mathematics operations, such as multiplication or addition. For instance, 50 HBW + 100 HBW or 50 HBW × 2 do not make sense. Conversion between the three hardness is possible with either the empirical formula or the regression of data from experiments [7]. A theoretical study for hardness conversion and tensile strength for materials that are ductile based on the evaluation of stress-strain curves is discussed in [8].

IIT or Depth-Sensing Indentation (DSI) is first introduced in [9]. In contrast to the aforementioned classical hardness measurement methods, since its early days, IIT has been developed so that it can work well with measurements carried out on thin films, coated profiles, or a variety of soft and hard metals [10]. This is possible because the method uses an indenter with a known geometry to indent a surface with incremental load or depth whose magnitude can be even to sub-micron resolution. During the process, the machine monitors the depth and normal force acting on the tip of the indenter as it is pressed and withdrawn from the tested surface. The result of the measurement is a curve of normal force (during loading-unloading cycles) versus the depth of the tip of the indenter, from which the hardness on a classic scale and the elastic modulus can be derived. Advances in modern technology have allowed us to measure the viscoelasticity and creep properties of the material using IIT in one run [11]. As the properties are measured in situ, the final indentation print is no longer necessary. Furthermore, the method can be highly automated and improved with different measurement and evaluation protocols, establishing a diverse regime for the development of IIT.

## 2.2 Digital Image Correlation

DIC is an optical, non-contact, Non-Destructive Test (NDT) method that is widely used to obtain the displacement fields on the surfaces of structures when being loaded [12]. Due to its nature, the method is highly applicable for testing environments with extreme conditions (highly corrosive, underwater, extreme strain, extreme temperature, etc.) [13, 14]. In comparison with strain gauge measurement, DIC is notably advantageous because it can realize full-field measurement, without the need for skillful installation and calibration of strain gauges. A typical setup for DIC measurement is composed of a high-resolution camera system (one or more), a lighting system, and a software for DIC control and post-processing [15]. Instead of physical strain gauges, virtual strain gauges can be created on the interested area via the software and appropriate full-field or local strain results can be extracted.

The method is based on the numerical form of an image, which is a matrix of pixels. By tracking the position of pixels in an image before (reference state) and after the loading condition is applied (strained state), ones can calculate the in situ displacement, from which the strain, stress, and other results can be obtained. It can operate in 2D mode (one camera) and 3D mode (multiple cameras). In order to realize the measurements, the surface at the area of interest must have a random visual so that the references for images can be taken. The patterns on the surface of the measured object can be either from its natural roughness or painted with white background and topped with arbitrary black dots (speckles) [13]. Owing to the simple setup requirement, DIC can be applied to almost all solid materials ranging

from metals, polymers, rocks, composites, ceramics [16], whether they are transparent or not, as long as they are visible to the DIC camera(s) during the measurement. A typical DIC setup is illustrated in Figure 2.2. The setup is used for measuring the strain field surrounding a semi-eclipse surface crack.
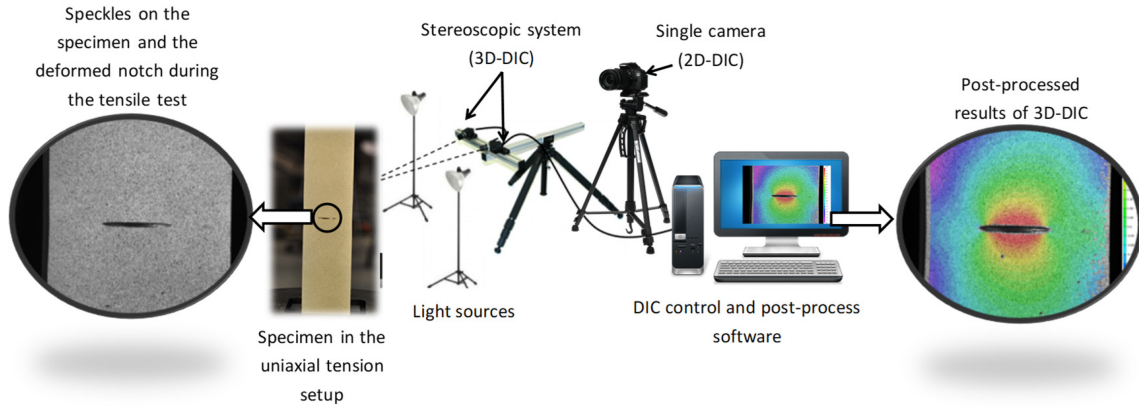


Figure 2.2: Example of a typical setup for DIC measurement [17].

Figure 2.2 shows the speckles on the surface of interest where there is the semi-eclipse crack. A high-resolution 2D camera records sequences of images and a post-processing software is used to evaluate the results. For 3D measurement, a stereoscopic system with two cameras is deployed. After capturing the sequential images, a contour map of the interest area showing the intensity of the strain can then be exported. The accuracy of DIC measurements depends on the Field of View (FoV), the number of pixels, and their numerical range (gray-scale resolution). The larger their numerical range, the better the difference between colors and the lighting condition is captured, leading to better pixel tracking [18]. By tracking the pixel blocks, it is possible to construct the full-field 2D/3D deformation vector fields. For more accurate DIC measurements, a number of software techniques have been investigated to better obtain sub-pixel resolutions. Nevertheless, this requires high computational time and memory usage because pixel-tracking tasks are conducted on images with much higher resolutions [19].

## 2.3 Finite Element Method

FEM is a numerical method used for approximating continuum mechanics, where a material is modeled as a continuous body to study its deformation and force transmission [20]. Methodologically, a continuum or a complete system is divided (discretized) into several smaller, countable (finite) connected parts (elements), whose behaviors are governed by a finite number of parameters. Then, the solution to the complete system The method can be calculated as an assembly of its elements. From the mathematical point of view, the large system described by Partial Differential Equations (PDE) is approximated with the discretization method (meshing) to form equations that are numerically simple to solve. Owing to its nature, FEM can be applied to a wide variety of complex continuum systems [21], such as the calculation of structures, fluid flow, heat transfer, electro-magnetics, vibro-acoustics,

etc. Because the results of FEM are approximated values solved by numerical approach, analyzers can tune the boundary values for the input to obtain results with a predefined accuracy level that meets their demand. For example, regarding the structural analysis, FEM can be used to solve the maximum stress that gear teeth experience under operation (Figure 2.3), which is impossible to be solved by an analytical approach.
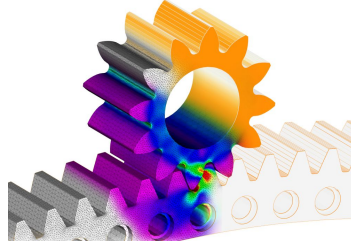


Figure 2.3: Example of a FEM result showing stresses on gears in contact [22].

As can be observed in Figure 2.3, FEM does this by constructing a mesh of finite pyramid-shaped elements that spans the geometry domain of the gear. Each finite element is formulated with necessary boundary values (geometry, loading condition, material properties, etc.), forming a simple equation. All the equations are assembled into a large system of equations that represents the entire gear. The final results are then approximated as FEM minimizes the error function by variation calculus. The results can then be reported by a contour map, where the red color indicates the maximum stress that the gear tooth experiences. Based on the stress distribution, the designers can implement necessary design changes to improve the strength of the components for a longer lifetime. For example, in the field of structural and stress analysis, FEM can be utilized to study the initiation of defects in railroad wheels during rolling contact [23], the connection of seats to the frame of rail wagon during impact [24], optimization of spring-loaded camming device [25], the load-bearing capacity of steel arch structure [26], the torsional stiffness of steel frame of formula car [27], etc.

## 2.4 Material models

For material models, it is essential to introduce basic definitions such as stress, strain, and other fundamental definitions [28]. Stress ($\sigma$) is used to quantify the effect of an external load on a body. For tensile loading, it is defined by the load over an area

$$\sigma = \frac{F}{A}, \tag{2.1}$$

where $F$ is the load and $A$ is the area the applied load is normal to. Similarly, strain ($\varepsilon$) quantifies the deformation in an infinitesimally small element of the body under the load. It is calculated by the change in length divided by the initial length

$$\varepsilon = \frac{L - L_0}{L_0}, \tag{2.2}$$

where $L$ is the elongation, and $L_0$ is the original length. If the stress is below the yield limit, the deformation is reversible when the stress is released. This linear elastic region is described by a parameter called Young's modulus ($E$)

$$E = \frac{\sigma}{\varepsilon}, \tag{2.3}$$

where $E$ is the slope of the line that connects point 0 with the yield limit, and is calculated following Hooke's law. The stress and strain in Equation (2.1) and Equation (2.2) are calculated assuming that the area $A$ remains the same during the whole test until failure. They are called engineering stress and engineering strain.

Indeed, the area gets smaller as the dog-bone specimen under the tensile test is elongated with tension applied on its both ends. This relative change in dimension is quantified by the Poission's ratio ($\nu$)

$$\nu = -\frac{\varepsilon_{trans}}{\varepsilon_{axial}}, \tag{2.4}$$

where $\varepsilon_{trans}$ is the strain in transversal direction, and $\varepsilon_{axial}$ is the strain in axial (longitudinal) direction. The minus sign indicates that the two strains are in opposite direction. For metallic material, empirical studies show that $\nu$ is often between 0.3 and 0.35. Given that the area changes in time, the engineering stress and engineering strain can be calculated into true stress ($\sigma_{true}$) and true strain ($\varepsilon_{true}$)

$$\sigma_{true} = \sigma(1 + \varepsilon), \tag{2.5}$$

and

$$\varepsilon_{true} = \ln(1 + \varepsilon). \tag{2.6}$$

From Equation (2.5) and Equation (2.6), it is possible to calculate the plastic strain ($\varepsilon_{pl}$) and the true plastic strain ($\varepsilon_{pl,true}$) as

$$\varepsilon_{pl} = \varepsilon_{total} - \frac{\sigma}{E}, \tag{2.7}$$

and

$$\varepsilon_{pl,true} = \ln(1 + \varepsilon_{pl}), \tag{2.8}$$

where $\varepsilon_{total}$ is the total engineering strain. Subtracting the elastic engineering strain component ($\sigma/E$) from it results in $\varepsilon_{pl}$ from which $\varepsilon_{pl,true}$ can be calculated. The natural logarithm is denoted as ln. Two values $\sigma_{true}$ and $\varepsilon_{pl,true}$ are essential for establishing the plasticity models of the materials.

In the field of material science and engineering, stress-strain curves (usually reported as engineering values) are the fundamental means for the evaluation of the mechanical properties of materials. A stress-strain curve is obtained by applying tension until failure on a predefined geometry with a known cross-section (usually dog-bone shape) along its longitudinal symmetrical axis. During the test, the load level and corresponding deformation are measured to calculate the uni-axial stress and strain levels as shown in Figure 2.4.

It can be observed in Figure 2.4 that as the stress grows versus strain on the tensile curve, it will first meet the proportional limit (A) and elastic limit/yield point (B). The 0A
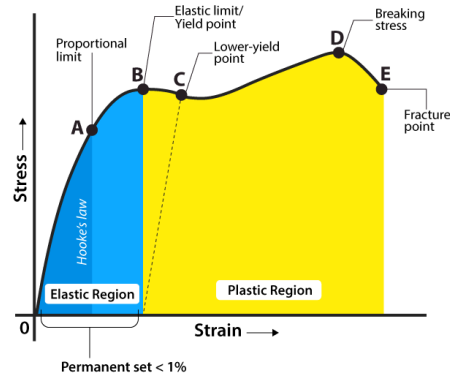
Figure 2.4: Example of a stress-strain curve with important key points [29].

span can be approximated with a line whose slope is calculated using Equation (2.3). As the stress continues to grow over point B, the deformation is not anymore fully reversible. Starting from the highest point of breaking stress (D), a phenomenon called necking happens and the fracture appears (E).

The 0B span is the elastic region. The BE span is the plastic region with the first portion BD being the strain hardening region, and the second portion DE being the necking region. If the stress is released within the elastic region, the deformation is fully reversed. If the stress level enters the strain-hardening region, permanent deformation occurs. In this region, piling up of dislocations (defects in the crystal lattice) happens and additional stress is required to additionally plastically deform the material. At this stage, the material appears stronger and harder. When the stress approaches the breaking stress, necking happens as the cross-section of the tensile specimen significantly reduces until the final fracture. For different materials, the stress-strain curves have different shapes as illustrated in Figure 2.5.
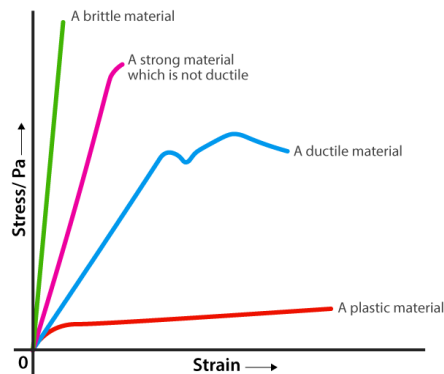


Figure 2.5: Example of different stress-strain curves for different material types [29].

It is clear now that the stress-strain curve in Figure 2.4 is applicable only for ductile material (blue curve). For brittle material, it does not experience necking as the stress level reaches the breaking stress, resulting in almost a straight line for the stress-strain curve (green and pink curves).

The stress-strain curve is important for engineers because it helps them to evaluate what kind of material they are working with and whether their designed component will fail or not under a given loading condition. It is worth mentioning that stress-strain curves obtained from the uni-axial tensile tests are applicable only for 1D cases. In practice, for the evaluation of metallic materials, 1D stress-strain data can be expanded to 2D or 3D cases by applying appropriate failure criteria [30], such as Rankine criterion (theory of maximum principal stress), Tresca criterion (theory maximum shear stress), von Mises criterion (theory of maximum distortion energy), and the theories of Coulomb-Mohr or Modified Mohr,etc. One failure criterion can better fit a material type than another based on empirical studies.

Material model or constitutive model is an equation that relates the stress (applied force) to the responding strain (responding deformation) or vice versa. It is one important input for FEM calculation. The behaviors of different materials are rather different from one to another, which are categorized into four ideal cases: elastic model, plastic model, viscoelastic model, and viscoplastic model [31]. The "visco" term refers to the viscous (fluidic) behavior. Elastic and plastic models do not depend on time (in other words, speed of deformation, strain rate), while viscoelastic and viscoplastic models do. The time dependence can be observed as one put a hand to water, the faster one does, the bigger the resistance of the water against the hand [31]. Within the framework of this section, only the plastic model is discussed, because it is applicable to a wide range of metallic materials (including steels in this study) and the interest is paid to modelling the plastic deformation under repeated indentation of IIT measurement. For material modelling, the hardening region can be approximated with a linear function, piece-wise linear function, or functions with higher orders as shown in Figure 2.6.
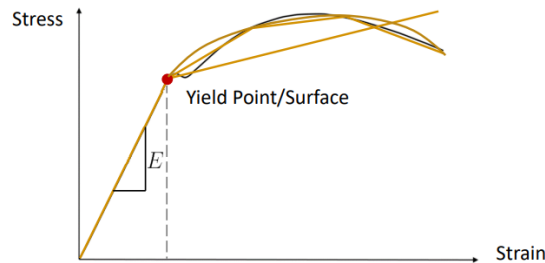


Figure 2.6: Hardening region approximated with different hardening functions [32].

For IIT, since the cyclic loading over the yield limit is involved, it is necessary to consider the two phenomena, i.e., isotropic hardening and kinematic hardening. Taking for example the 3D stress state and bilinear hardening model (where the hardening region is approximated with linear function), the two definitions can be illustrated in Figure 2.7.

The AB portion of the 1D stress state depicted on the right side of the figures corresponds to the monotonic uniaxial loading in a tensile test. On the left side, the cylinder shows the stress state in a 3D case with the base circle being the yield surface. For a material following isotropic hardening, when being loaded over the yield limit (point A), the yield surface is expanded to the yield stress (point B). When being unloaded in the opposite direction, the stress becomes 0 (load is completely released) and then negative (compressive)
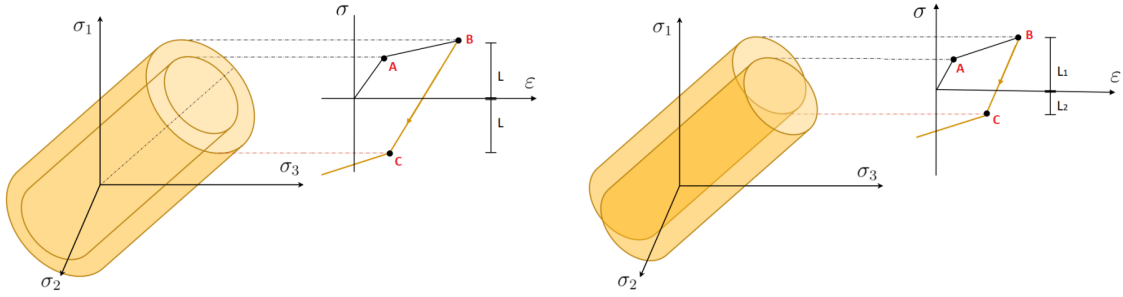
Figure 2.7: Two hardening models: isotropic hardening (left), and kinematic hardening (right) [33].

stopping at the other side of the yield surface (point C). Point B and point C are outside of the original yield surface.

While for material following kinematic hardening, the yield surface does not change in size but its origin is shifted. In this case, point B is outside the original yield surface but point C remains inside. In comparison with B, the yield stress at C in the opposite direction (compression) is reduced, which is called the Bauschinger effect [34]. For monotonic loading (portion AB), the behavior is the same for both types of hardening even though the 3D yield surfaces are different. However, for cyclic loading, they differ significantly because, after the first cycle, many other loading cycles are involved.

There is also the combined hardening, where the isotropic and kinematic hardening are combined, in which the yield surface both grows in size and its origin is shifted. This combined model is studied by Armstrong and Frederick [34] and later improved by Chaboche [35, 36]. Armstrong-Frederick (AF) model and its extension, Chaboche (CHAB) model, have been widely used by the commercial FEM code to describe the cyclic elasto-plastic behavior of materials under low cycle fatigue load or when the spring back effect is the interest of the study [37]. Hereby, just resulting constitutive relations for monotonic uniaxial loading and particular constitutive models are reported. By taking into account the initial values of plastic strain and backstress to be 0, the AF constitutive model is given as

$$\sigma = \sigma_Y + \frac{C}{\gamma}(1 - e^{-\gamma \varepsilon_{pl}}), \tag{2.9}$$

where $\sigma$ is the true stress, $\varepsilon_{pl}$ is the true plastic strain, $\sigma_Y$ is the yield limit, $C$ and $\gamma$ are material parameters. The AF model is easy to implement, however, cannot describe accurately the hysteresis loop in the case of cyclic loading. CHAB model solves this disadvantage by including the backstress components superposed of $M$ back-stress parts [38], then

$$\sigma = \sigma_Y + \sum_{i=1}^{M} \frac{C_i}{\gamma_i}(1 - e^{-\gamma_i \varepsilon_{pl}}). \tag{2.10}$$

The derivation of Equation (2.9) and Equation (2.10) can be found in [39]. To obtain the material parameters $C_i$ and $\gamma_i$, it is necessary to first choose the number of $M$ parts, then fit it with the $\sigma$ and $\varepsilon_{pl}$ calculated from the tensile test data. The curve fitting method that

is used in this study is the LSM [40]. It is a popular regression method that approximates functions by attempting to minimize the sum of the squared residuals. A residual stands for the difference between the fitted value that the model provides and the observed value.

From the mathematical point of view, Equation (2.10) resembles the Generalized Additive Model (GAM) whose degrees of freedom can be monitored to model highly complex non-linear data [41]. The AF model and its extension, CHAB model, are used to describe the strain-hardening behavior of the materials. Also known as work hardening, under a constant load rate, the higher the load or stress a material withstands, the stronger the material becomes. This owes to the formation and rearrangement of dislocations in the crystal lattice structure of the material. In general, this mechanism is captured with strain hardening models as an attempt to predict the change of mechanical properties because of plastic deformation.

Time-hardening models, on the other hand, are models that describe the hardening behavior of a material with respect to time. Under a constant load, the longer the time, the stronger the material becomes. This is because the dislocation density gradually increases in the crystal lattice structure of the material. As the material is stressed over time, more dislocations are formed and entangled with each other, making the material harder to deform. These models are useful for predicting the strength of components exposed to high temperatures and constant stresses over a long period, such as components of gas turbines, nuclear reactors, pressure vessels, steam pipes, etc.

Among the constitutive models that are used for describing the rate dependency of materials, there is the Perzyna model. It is a popular model used for the description of visco-plastic behavior. The primary feature of the model is to express the "overstress" effect, where the rate-independent yield function describing the visco-plastic strain can be higher than zero [42]. The Perzyna model is given as

$$\dot{\varepsilon_{pl}} = \gamma_v (\frac{\sigma_{eq}}{\sigma_y} - 1)^{\frac{1}{m}}, \tag{2.11}$$

where $\dot{\varepsilon_{pl}}$ is the accumulated (equivalent) plastic strain rate, $\gamma_v$ is the material viscosity parameter, $\sigma_{eq}$ is the equivalent stress and $\sigma_y$ is the yield stress of the material in static. The Perzyna model is a visco-plastic model used to describe the elastic-plastic and rate-dependent behavior of materials. In technical practice, it is possible to combine both the strain hardening model (CHAB) and the time hardening model (Perzyna) to describe both effects where significant plastic deformation and high strain rate are present, such as impact or explosion simulations.

## 2.5 Neural Networks

Machine Learning (ML) is a sub-branch of Artificial Intelligent (AI), which stands for the use of algorithms and data to replicate the learning process of humans on computers. It is a term that is first coined in [43] revolving around developing an autonomous checker program. Recent years have witnessed the tremendous growth of ML applications both for commercial and research purposes in the fields of computer vision, semantic analysis, prediction, natural language processing, and information retrieval [44].

An supervised ML method typically contains three consecutive components: a data processing procedure, an evaluation function, and an updating/optimization process [45]. A data processing module contains algorithms that intake data and attempt to predict or recognize patterns. The evaluation function monitors the accuracy of the model prediction. Evaluation function is so-called error/loss/fitness function [46]. An updating/optimization process tunes the parameters of the algorithms to reduce the error iteratively until a threshold error value is met [47].

There are four main ML methods: supervised learning, unsupervised learning, semi-supervised learning, and reinforcement learning [48]. Supervised learning takes labeled data as input and classifies them. Unsupervised learning takes unlabeled data as input and autonomously recognizes patterns, then classify them. Semi-supervised learning takes both labeled and unlabeled data as input and classifies them. Reinforcement learning employs a trial-and-error approach to find the optimal solution for a problem.

NN is a sub-branch of ML. First defined in [49], NN is a logical calculus that resembles the human nervous system. In the last decades, NN has been developed and employed to solve complex real-life problems that would take a considerable amount of computing resources to solve or that are unsolvable for human experts with traditional algorithms in various fields ranging from security to science, agriculture, manufacturing, education, marketing, etc. [50]. NN stands out from the rest of the traditional calculation methods due to the diverse approaches (different NN models) that it offers to work efficiently with large and complex datasets, yielding highly accurate and reliable results. A basic NN structure is depicted in Figure 2.8.
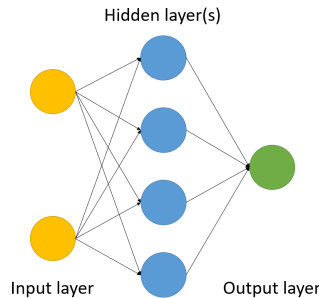


Figure 2.8: A basic NN structure with one input/hidden/output layer.

As can be observed in Figure 2.8, a basic NN is comprised of three layers: an input layer, a hidden layer, and an output layer. Layers contain nodes (neurons) and a node is connected to another with links. The input layer takes in the data and passes it through the hidden layer. After the evaluation is done, the result of the task can be taken in the output layer. A node is a fundamental processing unit of a NN that collects input and produces output. Figure 2.9 shows how inputs are calculated to produce an output.

As illustrated in Figure 2.9, inputs are collected and re-scaled by multiplying them with their corresponding connection weight. The summation of the weighted inputs is then added with a bias and passed through an activation function ($\varphi()$) to produce the output. The output then is in the form of $y = \sum_{i=1}^{n} x_i w_i + b$. In a NN with learnable parameters, the weights and biases can be updated during the training process to produce the desired
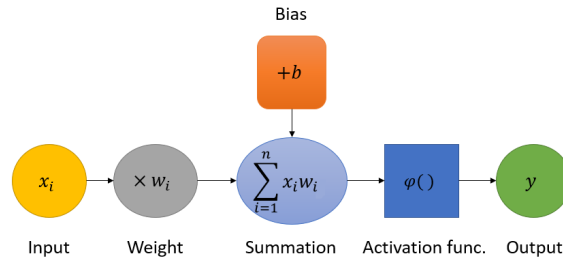
Figure 2.9: A basic neuron structure showing the calculation of inputs to an output.

outputs.

An activation function is a scalar-to-scalar function that calculates a net output of a node given an input or a set of inputs (output of multiple nodes). It defines the functional form of how a node should be activated to produce an output as the node has calculated the weighted sum and added the bias [51]. Among the most popular activation functions are sigmoid, tanh, Rectifier Linear Unit (ReLU), leaky ReLU, Exponential Linear Unit (ELU), softmax, softplus, etc. The shapes of these activation functions are depicted in Figure 2.10.
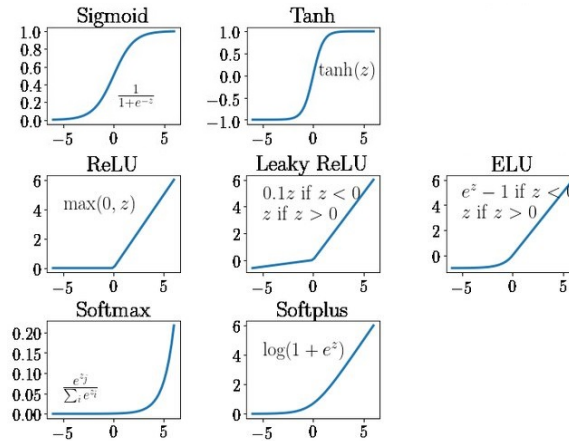


Figure 2.10: Examples of different activation functions [52].

The activation functions shown in Figure 2.10 are used to introduce nonlinearities into the NN [53]. It is essential for the training of the Feed-Forward Neural Network (FFNN) because the backpropagation algorithm needs to multiply the derivative of the activation function. Therefore, the chosen activation function has to be differentiable in order to be backpropagate-able. That is why sigmoid and other hyperbolic tangent functions have been widely adopted in the existing literature given that they can provide meaningful derivatives. Softplus, on the other hand, is a newer alternative that is differentiable and it is easier to demonstrate its derivative, in comparison with ELU [54].

The sigmoid function, which resembles an S, is used to convert variables that approach infinite to simple probabilities between 0 and 1. Most of the outputs are near 0 or 1. It has proven the capability to reduce extremely high or low values (outliers) in the dataset

without the need to remove them. This is applicable as well for tanh function. Whereas for other functions, such as softplus, produce the outputs from 0 to $+\infty$.

Depicted in Figure 2.8 is one of the most popular NN models, which is called FFNN. It is widely adopted in solving practical problems owing to its simple structure, easy implementation, and capability to recognize complex patterns in large datasets. A FFNN is a classification algorithm that contains forward connections between all the nodes without feedback connection [50, 55]. Each connection has a different weight value. During the information processing, data is entered from input nodes, then passes consecutively from one to another hidden layer to reach the output nodes. A layer is only connected to its previous layer and data is transmitted in one direction, from the inputs to the outputs [56]. If a NN is designed with more than two hidden layers, it is referred to as a Deep NN. The number of hidden layers and nodes in each hidden layer is arbitrary and is chosen depending on the complexity of the problem to be solved. A training process of a FFNN consists of the following steps:

Step 1: Weights initialization: the weight values between the nodes are randomly set.

Step 2: Forward propagation: data is input into the NN, with output of each node calculated using the weighted sum of its inputs and an activation function.

Step 3: Error calculation: the difference between the predicted output and the actual output (loss value) is calculated using a loss function (objective function).

Step 4: Backpropagation: the loss is propagated backward through the network and adjusted to minimize the loss value.

Step 5: Loss minimization: repeating Steps 2-3-4 for multiple runs (epochs) or until the loss value reaches a predefined threshold.

Loss function (or objective function) is a function that is used to compute the difference between outputs and their corresponding expected outputs. The subject for an optimization problem is to minimize the loss function or maximize its negative. In the context of NN, a loss function attempts to calculate how close the values predicted by NN are to their true counterparts [57]. The errors are calculated for all the predictions over the dataset and then averaged then to a single number that represents the performance of the NN. For continuous variables, mean square error (or LSM) is often chosen as a loss function, while for binary and ordinal outcomes, hinge loss, poisson loss, or logistic loss are used [51].

For most of the problems that need NN, it is impossible to find an exact analytical solution but rather an approximated one using an iterative optimization algorithm to minimize the loss function, for example, gradient descent, stochastic gradient descent, and adaptive moment estimation [58, 59]. Given for example the Adam optimization algorithm [60], it is a stochastic gradient descent method based on adaptive estimation of first-order and second-order moments. The method requires minimal memory, remains invariant to the diagonal rescaling of gradients and thus is computationally efficient and highly applicable for problems with large datasets/parameters [61]. For the mentioned FFNN, backpropagation is a technique to calculate the gradient in the NN, while the method for updating the loss value can be one of the listed optimization algorithms. It should be noted that backpropagation is applicable not just to FFNN or NN in general. For different problems or different NN such

as a Recurrent NN (RNN), it can be a good fit as well.

Indeed, NN has been combined with FEM to predict the mechanical properties of materials from IIT results (usually F-D curves). Traditionally, the IIT test produces F-D curves from which empirical formulas can be applied to calculate the material properties [62]. However, it is subject to difficulties with the work-hardening phenomenon when excessive pile-up/sink-in effects exist [63]. Therefore, it is possible to avoid these drawbacks by employing FEM (with a given material model) to simulate several IITs from which F-D curves are collected. These curves are then used to train a NN. The trained NN is then used to predict the parameters of the material model. In [63] the calculation of material parameters using NN in combination with FEM is referred to as an inverse approach. Using the inverse approach, it is possible to predict the uniaxial tensile flow [64], nanomechanical properties [65], and residual stress [66].

Specifically, authors in [64] employ NN to predict the tensile properties of six types of steels: lean duplex, ferritic-bainitic, dual-phase, transformation-induced plasticity, and austenitic stainless steel. The Taguchi orthogonal array method is used to reduce the training data pairs while being able to provide prediction with high efficiency and accuracy (controlled below 1%). Besides, reported in [65] is the combination of nanoindentation and NN to determine the nanomechanical properties. Specifically, a database of material properties such as yield strength-to-modulus ratio, coefficient for work hardening, Poisson's ratio, and indentation angle are collected. The proposed NN is trained with this database and later used to predict the aforementioned parameters by taking F-D relationship as input. The authors validate the proposed solution for a wide range of steel and aluminum. In [66], authors attempt to predict the equi-biaxial residual stresses and mechanical properties of an aluminum plate. The compare the k-nearest neighbor (a supervised ML model) with the Kriging model and prove that the former performs slightly better in terms of prediction accuracy for such a task.

# Chapter 3

# Physical tests

## 3.1 Surface roughness measurement

### 3.1.1 Measurement setup

The specimen for IIT is cut from a cold-drawn SS304L bar. It is cylinder-shaped with a height of 10 mm. On one side, the circular surface is machined and grinded to meet the roughness requirement for the IIT test following the traditional Brinell test - ISO 6506 [67]. Ball indenter has the advantage of averaging out the hardness differential due to surface irregularities owing to its large area. Besides, a spherical shape ensures that the force application is always normal to the tested surface and relatively consistent within the testing period. By the rule of thumb, an areal average roughness (Sa) of 2 $\mu$m is sufficient for proper hardness measurement.

### 3.1.2 Results

The surface roughness of the specimen is inspected with Alicona Infinite Focus 5G optical microscope from Alicona Imaging GmbH. The area to be sampled is 1.614 mm x 1.610 mm resulting in the true area of 2.597 mm$^2$. The number of measured points in this area is 3,348,896. The surface roughness results are shown in Figure 3.1.
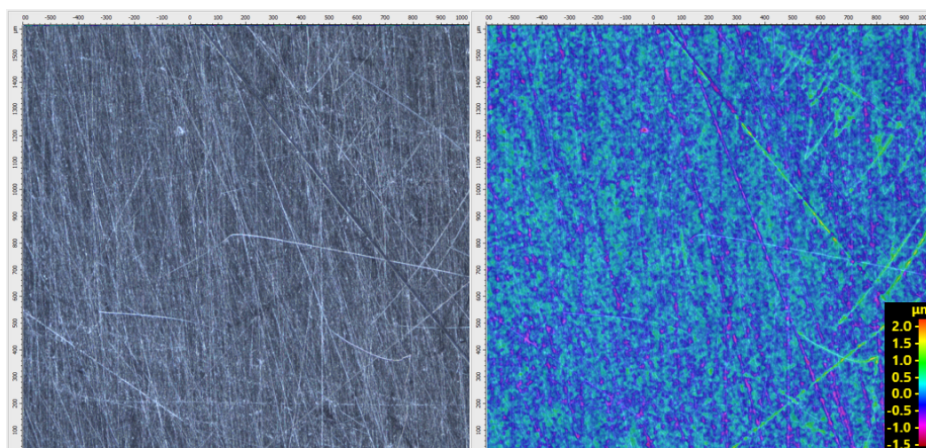


Figure 3.1: Surface roughness measurement: close-up view (left), and contour map of the surface (right).

As shown in Figure 3.1, the inherits the marks from the cutting tool and scratches as it is stored together with other specimens. The maximum and minimum roughness is respectively 2.241 $\mu$m and -1.539 $\mu$m. The Sa value is 0.193 $\mu$m. The surface roughness satisfies the requirement for the subsequent hardness test. Besides, it should be noted that the surface should be even and free of dust, lubricants, and any oxide scale to facilitate accurate measurement of the ball indenter's diameter. Any surface alteration resulted from heat-working or cold-working has to be avoided because it introduces a layer of hardened material which is unfavorable for IIT test. This means that if the IIT measurement is conducted on a machine's component in situ, it is necessary to remove the painted/hardened/oxidated/scratched outer layers while keeping it clean from other foreign matters.

## 3.2  Instrumented Indentation Test

### 3.2.1  Measurement setup

The machine used for IIT is PIIS 3000 from UTM company [68]. The machine is portable, fully automatic, and designed for testing the mechanical material properties, fracture toughness, and weld residual stress of structural components operating under industrial conditions (in situ). The machine follows the standards B0950, B0951, ISO/TR 29381, KEPIC code MDF A370 and ASME Code case 2703.

The indenter is made of carbide material with $E = 624$ GPa at 23℃. The transducer is 4 mm above the indenter. The measurement starts with a depth of 0 mm when the contact force is detected to be 2 N. The period taken for each step is relatively long to avoid any undesired change of material related to rapid load or temperature changes. The machine is kept free from shock and vibration during the measurement. The test setup and result are shown in Figure 3.2.



Figure 3.2: UTM test setup (left) and IIT results for the SS304L sample (right).

As can be observed in Figure 3.2, the hardness specimen is machined on the bottom side with two perpendicular faces to facilitate better clamping on the jig. Since the machine is fixed on its frame, multiple IIT measurements are realized by moving the jig under the indentation ball. The hardness test is carried out along the diameter and it is possible to observe the imprints of all the tests. The positioning is realized manually aiming at having an

adequate distance between the test imprints (the holes) while attempting to keep them in a straight line. The distance is maintained so that the build-up or shrink-in effect surrounding a test imprint does not influence the result of another.

### 3.2.2 Results

There is no visible deformation on the back surface of the specimen. It indicates that the height of 10 mm is sufficient for the IIT and the results are free from the influence of the specimen's thickness. Indeed, the thickness of the test piece should be at minimum eight times the depth of the indentation (150 $\mu$m), which is applicable for the case herein. The PIIS machine automatically exports the F-D curves in .csv format. The imprints are numbered from left to right following Figure 3.2 with point 6 at the middle of the measured line. The F-D results are collected and plotted in the same graphs for easier comparison as shown in Figure 3.3.
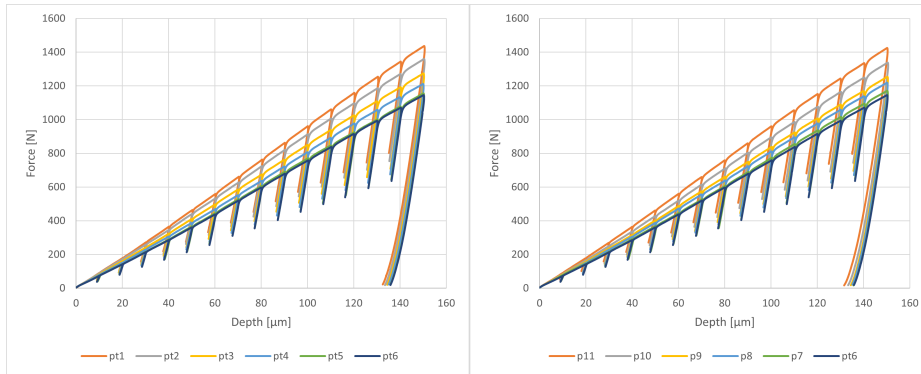


Figure 3.3: F-D curve results from IITs of the SS304L sample: from point 1 to point 6 (middle point) (left), and from point 6 (middle point) to point 11 (right).

As can be observed in Figure 3.3, the maximum force is the highest at the points situated furthest from the center (near the outer edge) and gradually reduces as the indenter head is moved toward the center. This indicates that the specimen under investigation has harder outer layers and is thus in-homogeneous. As for the tensile specimen, the outer layers of the bar are machined out, leaving alone the core with the weakest strength. The difference in hardness corresponds to the fact that the material is cold-drawn, leading to increased hardness in the outer layers. Thus, the tensile results and the IITs are comparable only in the middle of the bar. This is valid for this study, because the tensile specimens are subjected to turning process that machines out only the outer layers of the material which are hardened. However, for a more appropriate study, the chosen material should be homogeneous, so that IIT and tensile test results are comparable.

## 3.3 Digital Image Correlation measurement

### 3.3.1 Measurement setup

The tensile specimens are machined by the turning method from the same billet that is used for IIT. For DIC measurement, the samples have to be painted first with white background and black dots as can be observed in Figure 3.4.



Figure 3.4: Preparation of specimens for tensile test with DIC measurement.

As shown in Figure 3.4, the two grip sections are covered with tape to avoid being painted, so that the specimens are not slippery when being gripped by the grippers. The tensile test is carried out at room temperature with a hydraulic machine LabControl 100 kN/1000 Nm following ISO 6892-1 standard. The used position rate is 10 mm/min and the specimens are tested to failure.

The position change of the black patterns on the gauge section is monitored by a camera and calculated to strain using the software MERCURY RT. In order to do so, it is necessary to first calibrate the camera with the software, then create a virtual probe to capture the longitudinal strain. Notably, the position of the probe must be visible by the camera during the whole testing period so that the initial, as well as the elongated length, can be recorded. The setup for the DIC measurement can be seen in the following Figure 3.5.
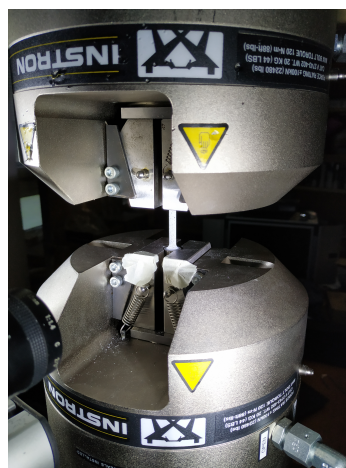


Figure 3.5: Setup of tensile test for a SS304L specimen with DIC measurement.

In Figure 3.5, it is possible to observe that the specimen is gripped so that the gauge section is visible to the camera. A flashlight is installed to provide sufficient illumination for the image recording process. The extra tapes on the bottom grips are applied to prevent redundant reflection, which caused the software to fail in recognizing the virtual probe. In this study, five specimens are tested with the position rate of 10 mm/min from which the average results and standard deviation are calculated. Additionally, two extra samples are tested, one with 1 mm/min and one with 100 mm/min.

### 3.3.2 Results

The surface of the specimen under tensile test is recorded. Owing to the pattern movements in each consecutive image frame, the software can track the axial displacement and calculate the axial strain of the specimen. From that, it is possible to export a contour map for better visualization. However, in this study, it is sufficient to report the unprocessed snapshots of the DIC measurement as in Figure 3.6.
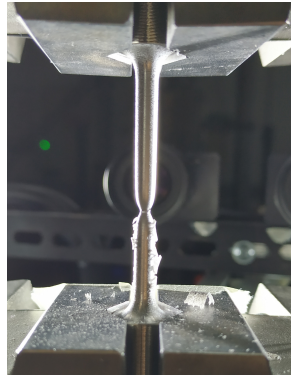


Figure 3.6: A broken SS304L tensile specimen monitored with DIC measurement.

The specimen broke in the middle, which is ideal for tensile test because it showed that the specimen is machined properly so that no defect appears near its shoulders. The failure in the middle is observed as well for four other specimens. What can be drawn from the failure mode is that the material is highly ductile (necking and considerable elongation). The highlights of the specimens under the tensile test are depicted in the following Figure 3.7.

As can be seen from Figure 3.7, the initial virtual strain gauge is stretched and disappeared after the specimen is broken. There are breakages of the painting that appear in the form of horizontal cracks along the gauge length of the specimen. In the last figure, the necking phenomenon indicated that the material under testing is ductile. Indeed, SS304L is a highly ductile material owing to the high composition of Chromium. The optical microscope Alicona InfiniteFocus 5G is used to capture the fracture in detail. The close-up view of the fracture of the tensile specimen is shown in Figure 3.8.

Figure 3.8 shows a significant reduction of the cross-section due to necking, indicating that the material is highly ductile. Moreover, it is remarkable that the outer surface of the sample resembles the staircase that it inherits from the turning process. Judging from the failure of the sample (fracture in the middle) as well as the shape of the necking, it can be
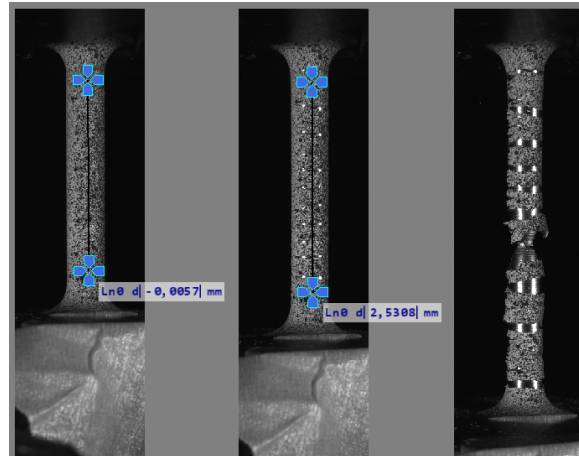
Figure 3.7: Failure of a SS304L specimen under tensile test: original shape (left), elongation under testing (middle), and broken specimen (right).
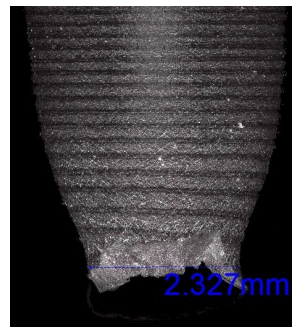


Figure 3.8: Close-up view of the fracture of the SS304L tensile specimen.

drawn that the tool's imprints affect the tensile results. However, how significant the effect is is not the subject of this study. Rather, the thesis aims to establish first the framework that integrates the FEM in combination with NN and refines the material inputs later. A property that is more significant for this study is the dependency of the material on the strain rate (strain rate sensitivity). The stress-strain curves of the material tested under three different strain rates are plotted in Figure 3.9.

It can be concluded from Figure 3.9 that different strain rate does not affect much the yield limit while considerably reducing the ductility of the material. The mechanical properties evaluated from these three tests are reported in Table 3.1.
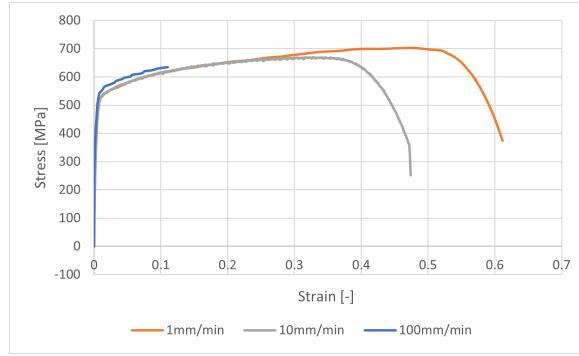
Figure 3.9: Effect of different strain rate on the stress-strain curve of the material.

Table 3.1: Material properties from tensile tests for three different strain rates.

| Test speed | $E$ [MPa] | $\sigma_y$ [MPa] | $\sigma_u$ [MPa] | $\varepsilon_u$ [-] | $\varepsilon_{max}$ [-] |
|---|---|---|---|---|---|
| 1 mm/min | 180203 | 439 | 702 | 0.48124 | 0.61128 |
| 10 mm/min | 184896 | 436 | 670 | 0.32687 | 0.47393 |
| 100 mm/min | N/A | N/A | 635 | 0.11026 | 0.11026 |

In Table 3.1, there are $E$, yield strength $\sigma_y$, ultimate strength $\sigma_u$, ultimate strain $\varepsilon_u$ corresponding to $\sigma_u$, and the strain at fracture $\varepsilon_{max}$. It should be noted that non-applicable (N/A) marking is because of the data missing from tensile tests. Herein, the results of 10 mm/min are chosen for the study because it is in general the most common strain rate that the technical components made of this material would meet in reality, instead of the two other extreme conditions, too slow (1 mm/min) or too fast (100 mm/min).

# Chapter 4

# Finite Element Method

## 4.1 Material model

### 4.1.1 Calibration of Chaboche model

First, to simulate an indentation test using FEM, there is a need to find a constitutive model that describes the plastic behavior of the material under testing. From the tensile data, a set of points governing the relationship between true stress and true plastic strain can be calculated and later fitted with LSM to a chosen constitutive model such as CHAB. Employed in this study are two variants of CHAB model whose formulas are shown as follows. The first variant is

$$\sigma = \sigma_y + C_2\varepsilon_{pl} + \frac{C_1}{\gamma_1}(1 - e^{-\gamma_1\varepsilon_{pl}}), \tag{4.1}$$

that corresponds to

$$\sigma = b_0 + b_1\varepsilon_{pl} + b_2(1 - e^{-b_3\varepsilon_{pl}}). \tag{4.2}$$

Besides, there is

$$\sigma = \sigma_y + \frac{C_1}{\gamma_1}(1 - e^{-\gamma_1\varepsilon_{pl}}) + \frac{C_2}{\gamma_2}(1 - e^{-\gamma_2\varepsilon_{pl}}), \tag{4.3}$$

that corresponds to

$$\sigma = b_0 + b_1(1 - e^{-b_2\varepsilon_{pl}}) + b_3(1 - e^{-b_4\varepsilon_{pl}}). \tag{4.4}$$

Equation (4.2) and equation (4.4) are re-formulated with variables from $b_0$ to $b_4$ to use for curve fitting in Python for simpler computation. Three functions are named and used for curve fitting studies. Specifically, Equation (4.2) is function CHAB4, Equation (4.4) is function CHAB5Y and function CHAB5. Function CHAB5Y differs from CHAB5 because the first variable $b_0$ is fixed with the $\sigma_y$ value of 436 MPa. After the curve fitting using Python, the variables from $b_0$ to $b_4$ are obtained and listed in Table 4.1. The fitted variables in Table 4.1 are calculated according to Equation (4.1) and Equation (4.3) to obtain the material parameters in Table 4.2.

Table 4.1: Curve fitted variables for CHAB with different number of parameters.

| Model | $b_0$ [MPa] | $b_1$ [MPa] | $b_2$ | $b_3$ [MPa] | $b_4$ |
|-------|-------------|-------------|-------|-------------|-------|
| CHAB4 | 480 | 1158 | 91 | 50 | 0 |
| CHAB5Y | 436 | 838 | 2 | 103 | 182 |
| CHAB5(1) | 330 | 784 | 2 | 205 | 357 |
| CHAB5(2) | 330 | 205 | 357 | 784 | 2 |

Table 4.2: Curve fitted variables recalculated to material parameters.

| Model | $\sigma_y$ [MPa] | $C_1$ [MPa] | $\gamma_1$ | $C_2$ [MPa] | $\gamma_2$ |
|-------|------------------|-------------|------------|-------------|------------|
| CHAB4 | 480 | 4550 | 50 | 1158 | 0 |
| CHAB5Y | 436 | 1676 | 2 | 18746 | 182 |
| CHAB5(1) | 330 | 1568 | 2 | 73185 | 357 |
| CHAB5(2) | 330 | 73185 | 357 | 1568 | 2 |

From CHAB5 model, there are two variations CHAB(1) and CHAB(2). CHAB5(1) has $C_1$ and $\gamma_1$ lower than $C_2$ and $\gamma_2$ while CHAB5(2) is vice versa. The reason for the existence of CHAB5(1) and CHAB5(2) functions is that they return the same curve-fitting plot. This is acceptable from the mathematical point of view and defining the material model in ANSYS APDL with either CHAB(1) or CHAB(2) will return the same results. However, it is not correct in terms of material model, because in CHAB model with five parameters, the two parameters of the first nonlinear component ($C_1$ and $\gamma_1$) should be greater than those of the second nonlinear component ($C_2$ and $\gamma_2$). Therefore, only the parameter set for CHAB5(2) is considered for CHAB5. The curve fitting results for the three functions are presented in Figure 4.1.
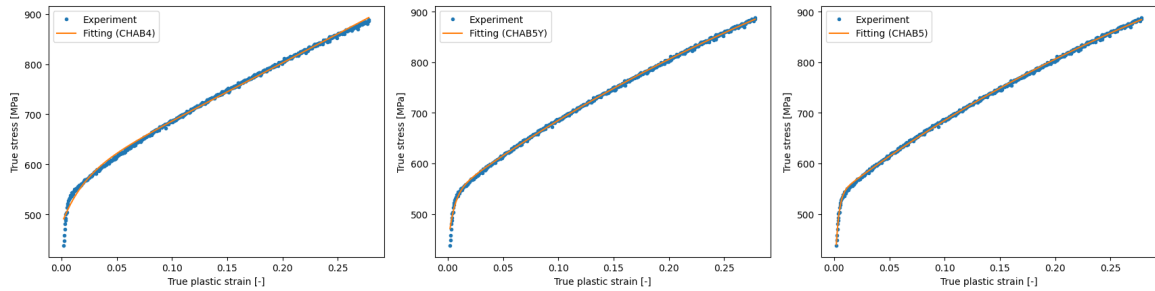


Figure 4.1: Fitting results of CHAB models with different number of parameters.

The three fitted curves plotted in Figure 4.1 approximate relatively well the stress value where the true plastic strain is over 0.05. A close-up view of the yield region approximated by the three functions is presented in Figure 4.2.
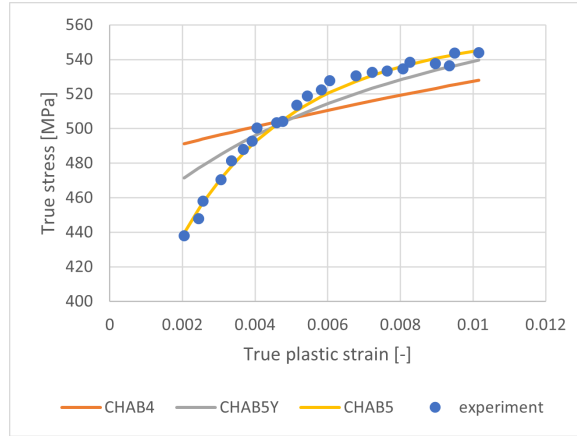
Figure 4.2: Comparison of CHAB models with different number of parameters for their ability to approximate the yield region.

As can be observed in Figure 4.2, the curvature portion near the yield region (with plastic true strain value between 0.002 and 0.01) could not be approximated with CHAB4 function following Equation (4.1). Therefore, it is necessary to add another nonlinear term to the origin CHAB4 function to better approximate that portion, thus, the reason for using CHAB5Y function and CHAB5 function following Equation (4.3). Subsequently, it can be drawn that the CHAB5 function is the most suitable function for the SS304L material used in this study.

### 4.1.2 Calibration of Perzyna model

The Perzyna model can be combined with a kinematic hardening model such as CHAB to describe the time dependency of the material. However, it should be noted that if Perzyna is employed, the CHAB model must be fitted with the tensile result from the lowest position rate, which is 1 mm/min, as opposed to the tensile result from 10 mm/min is fitted with CHAB5 above. Even though the Perzyna model calibration is reported here, it serves only as a possible direction for future work where strain-rate sensitivity can be considered. For IIT simulation in this study, the tensile data from the test of 10 mm/min is utilized instead of the 1 mm/min because it is closer to the testing speed of the real machine.

For calibration of the Perzyna model, it is necessary to start with the tensile result of the lowest strain rate, which will serve as a reference for further calculation. First, the plastic strain rate for the testing speed of 1 mm/min is calculated. By plotting the true plastic strain versus time, the plastic strain rate can be obtained as shown in Figure 4.3.

The slope of the curve obtained by linear fitting in Figure 4.3 is the plastic strain rate, which is $\dot{\varepsilon}_{pl,1} = 0.04828$ %/s. This calculation procedure is applicable as well for the test results of 10 mm/min and 100 mm/min and the results are respectively $\dot{\varepsilon}_{pl,10} = 0.4828$ %/s and $\dot{\varepsilon}_{pl,100} = 4.828$ %/s. Furthermore, it is necessary to collect the engineering stress at 1% engineering strain ($\sigma_{\varepsilon_1\%}$) and the corresponding plastic strain ($\varepsilon_{pl_1\%}$). Moreover, calibrating the combination of CHAB and Perzyna models requires as well the true stress
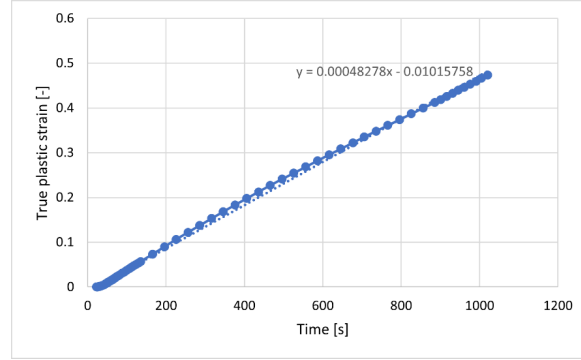
Figure 4.3: The plastic strain rate of tensile test with the lowest strain rate of 1 mm/min.

calculated at 1% engineering strain using CHAB5 model ($\sigma_{CHAB,\varepsilon_1\%}$). As aforementioned, the CHAB5 model is used but the fitting is realized on the tensile test with the lowest position rate (1 mm/min). The procedure is the same but a different set of material parameters is calculated, that is, $\sigma_y = 250$ MPa, $C_1 = 60775$ MPa, $\gamma_1 = 325$ MPa, $C_2 = 1463$ MPa, and $\gamma_2 = 0.67$. Then $\varepsilon_{pl_1\%}$ and an intermediate variable $x$ are calculated as follows

$$\varepsilon_{pl_1\%} = 0.01 - \frac{\sigma_{\varepsilon_1\%}}{E}, \tag{4.5}$$

$$x = \frac{\sigma_{\varepsilon_1\%} - \sigma_{CHAB,\varepsilon_1\%}}{E}. \tag{4.6}$$

Utilizing Equation (4.5) and Equation (4.6) results in Table 4.3. Variable $x$ is then plotted versus $\dot{\varepsilon}_{pl}$ for three different strain rates and conduct curve fitting with power law to show the equation that governs their relation in Figure 4.4.

Table 4.3: Parameters for calibration of Perzyna model.

| Test speed | $\dot{\varepsilon}_{pl}$ [s$^{-1}$] | $\sigma_{\varepsilon_1\%}$ [MPa] | $\varepsilon_{pl_1\%}$ [-] | $x$ |
|---|---|---|---|---|
| 1 mm/min | 0.00048 | 525 | 0.00708662 | 0.731721 |
| 10 mm/min | 0.0047 | 527 | 0.00707552 | 0.741721 |
| 100 mm/min | 0.047 | 548 | 0.00695899 | 0.846721 |

By fitting three points in Figure 4.4 with power law, $m = 0.0319$ and $1/\gamma_v^{1/m} = 0.9153$ are obtained. From these, two Perzyna parameters, that is, $m = 0.0319$ and $\gamma_v = 16.029$ are calculated. The viscoplastic stress $\sigma_{vp}$ can be calculated for three different strain rates using formula

$$\sigma_{vp} = \sigma_y \left(\frac{\dot{\varepsilon_{pl}}}{\gamma_v}\right)^m. \tag{4.7}$$

The viscoplastic stress for three cases, respectively, for 1 mm/min, 10 min/min, and 100 mm/min are $\sigma_{vp,1} = 143$ MPa, $\sigma_{vp,10} = 154$ MPa, and $\sigma_{vp,100} = 166$ MPa. These viscoplastic stress components are summed up with the true stress calculated with CHAB5
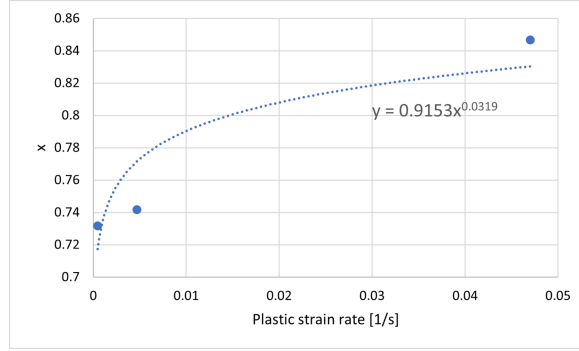
Figure 4.4: The relation between $x$ and $\dot{\varepsilon_{pl}}$ for calibration of Perzyna model.

for 1 mm/min ($\sigma_{CHAB}$) to obtain the total true stresses for three different strain rates following

$$\sigma_{total,1} = \sigma_{CHAB} + \sigma_{vp,1}, \tag{4.8}$$

$$\sigma_{total,10} = \sigma_{CHAB} + \sigma_{vp,10}, \tag{4.9}$$

$$\sigma_{total,100} = \sigma_{CHAB} + \sigma_{vp,100}. \tag{4.10}$$

The analytical solutions $\sigma_{total,1}$, $\sigma_{total,10}$, and $\sigma_{total,100}$ are plotted versus $\varepsilon_{pl,true}$ and fit well with the experimental results. To simulate and calibrate the time-dependent viscoplastic model, a 3D cube with sides of 1 mm, which is meshed with one linear BRICK185 element. The material parameters are $E$, $v = 0.3$ (linear isotropic); $C_1$, $C_2$, $C_3$, $C_4$, and $C_5$ corresponding respectively to $\sigma_y$, $C_1$, $\gamma_1$, $C_2$, and $\gamma_2$ (CHAB kinematic hardening); $m$ and $\gamma$ (rate-dependent visco-plasticity, Perzyna model).

This FEM model functions so that when one can simulate the time-hardening phenomenon by changing the time for simulation. The time is calculated from the test speed respectively for 1 mm/min, 10 mm/min, and 100 mm/min to be 24 s, 2.4 s, and 0.24 s. The displacement is 40%, which is approximated from $\varepsilon_u$. The true stress-true (total) strain curves for three different strain rates are shown in Figure 4.5.
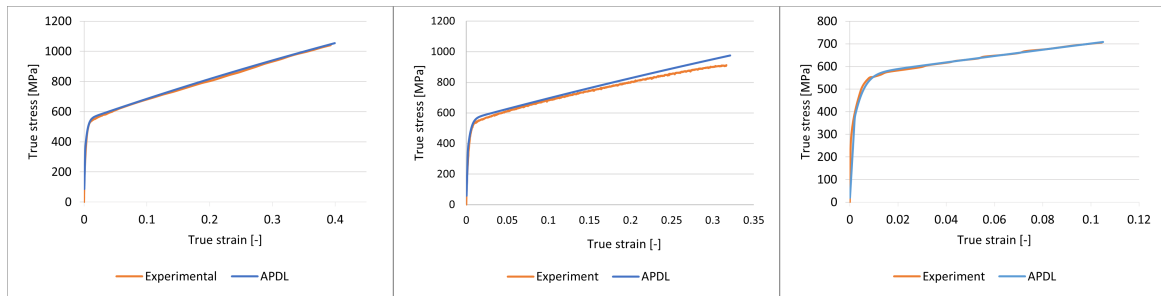


Figure 4.5: Comparison of true stress-true strain curves obtained from experiments and ANSYS APDL: 1 mm/min (left), 10 mm/min (middle), and 100 mm/min (right).

From Figure 4.5, it can be observed that the Perzyna model is well calibrated with reality for the herein SS304L material. The material setting can be used for simulations of

more complicated components. It should be noted as well that the Perzyna model is not employed for the simulation of IIT in this study because the indenting speed is relatively low. Therefore, it is sufficient to work with the tensile results from the test speed of 10 mm/min.

## 4.2 Simulation in ANSYS APDL

The scripting is prepared in ANSYS Mechanical APDL 2019 R1. The geometry is chosen to be 1 mm x 1 mm square deformable 2D plane indented by a rigid 2D circle representing the ball indenter of 1 mm in diameter. To save computational time, 2D axisymmetric simulation is employed. The simulation setup is based on [1].

### 4.2.1 Meshing

First, the meshing strategy for the cube is decided as depicted in Figure 4.6. The edges with the same letter marking (a, b, c) have the same number of nodes. Marking for the nodes is also applied in the APDL script. The meshing strategy is based on [69].
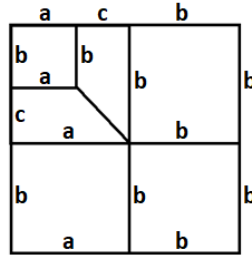


Figure 4.6: Meshing strategy for IIT simulation.

From Figure 4.6, it should be noted that the mapped meshing is applicable only for four-sided faces. Therefore, any splitting that results in faces with more or less than four sides will fail the meshing machine. After defining the number of nodes on the sides, the geometry is meshed with 2D elements (PLANE182). The element type is linear. Due to the node distribution in the previous step, the area under the indenter is refined with smaller elements after meshing as shown in Figure 4.7.

The meshed geometry in Figure 4.7 subjects to the indentation of a ball indenter driven by a pilot node at the center. This node is used to collect the reaction force as well as the depth to form the F-D curve, which is the backbone of the whole study. The contact type is Surface-to-Surface (CONTA172) between the rigid indentation ball geometry (TARGE169) and a deformable 2D cube (PLANE182). The contact algorithm is Augmented method. The pilot node is assigned with a high ID (99999) so that it does not coincide with any other node if the geometry is going to refined with a bigger number of elements.

In this example, the edges a, b, and c are meshed respectively with 10, 12, and 8 divisions. For the first trial, there is only one loading cycle during which the indenter is
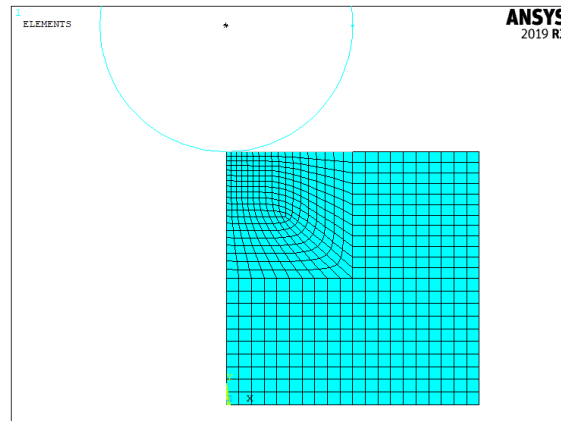
Figure 4.7: Meshed geometry and setup for IIT simulation.

pressed down from 0 to 150 $\mu$m without any middle unloading like in the real IIT. The von Mises (equivalent) stress (VMS) contour is shown in Figure 4.8.
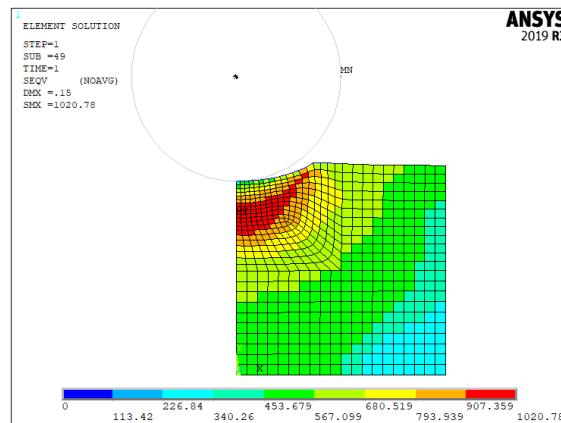


Figure 4.8: VMS result after for one loading-unloading cycle.

The VMS distribution in Figure 4.8 follows the Hertz contact [70]. Specifically, the maximum stress is below the contact surface. The maximum VMS recorded at the region with red contour is 1020 MPa. It should be noted that the more the mesh is refined, the better the resolution of the contour is. However, this comes at the cost of significantly longer computational time. The mesh study is shown in Table 4.4.

Table 4.4: Effect of mesh size on simulation for one loading-unloading cycle.

| a | b | c | Element | Time [s] |
|---|---|---|---------|----------|
| 10 | 12 | 8 | 636 | 25 |
| 20 | 24 | 16 | 2502 | 112 |
| 40 | 48 | 32 | 9930 | 490 |

As shown in Table 4.4, by increasing the number of nodes on side a, b, and c, the number of elements and the time for calculation increases by many folds. Finer mesh leads to better contour mapping and a smoother F-D curve, but the maximum VMS remains approximately 1020 MPa and the maximum force on the F-D curve is the same. Notably, to simulate the real IIT, one has to simulate 15 loading-unloading cycles, which will significantly prolong the time for simulation.

### 4.2.2 Boundary condition

Regarding the movement of the indenter, after indenting for 10 $\mu$m, the indenter is withdrawn 5 $\mu$m so that the elastic component (stress/strain) can be released, leaving alone the plastic component. This is done to facilitate the analytical stress-strain calculation later on as described in [1]. In APDL simulation, the displacement of the ball indenter versus time can be set as shown in Figure 4.9.
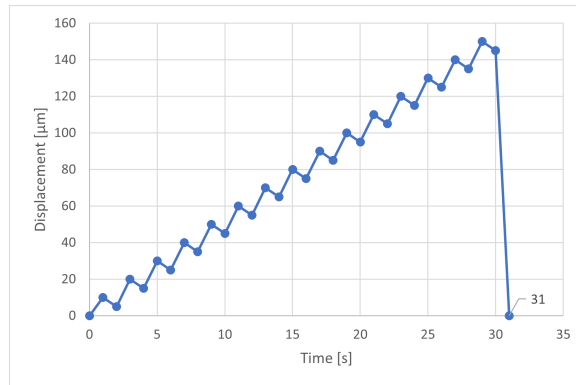


Figure 4.9: Movement of the ball indenter for 15 loading-unloading cycles.

In fact, the movement of the indenter in Figure 4.9 does not follow the real setup of the IIT machine. The IIT machine is programmed so that after 10 $\mu$m of indenting, the indenter is withdrawn for 50 % of the in situ measured load. These two actions form one loading-unloading cycle and are repeated until the indenter tip reaches 150 $\mu$m. With regard to the geometry and coordinate system in Figure 4.7, three different types of boundary conditions are investigated as illustrated in Figure 4.10.

In the first case, the material sample is sized 1 mm x 1 mm with one symmetric boundary condition (fixed movement in Ox axis) in the left edge and one fixation (fixed
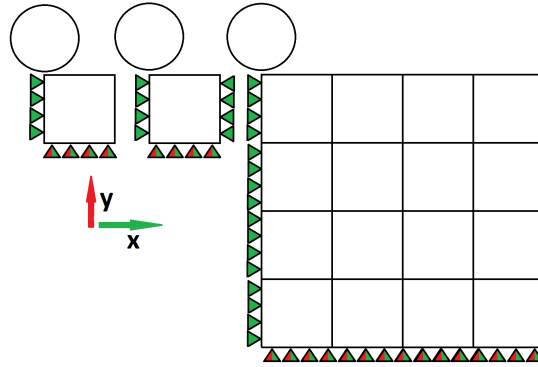
Figure 4.10: Different boundary conditions for IIT simulation.

movements in both Ox and Oy axes) in the bottom edge. Besides, two more cases are considered. The second case is with extra constraint in Ox axis in the right edge. The third case is with wider sample size, resembling best the reality in which the diameter of the indenter is considerably small in comparison with the size of the test sample.

The reason for considering the second and third cases is that in the first case, the right (free) edge can still deform, which may not present the reality where it is surrounded by much thicker material. Adding an additional constraint in the free edge (second case) or widening the free edge (third case) would introduce the effect of the rigid material surrounding the stressed area to the simulation. After comparison, the most appropriate boundary condition is the second case, regarding that fact that the number of elements can be significantly reduced while not sacrificing so much the accuracy in comparison with the third case. The boundary conditions in the second case are chosen and applied throughout the whole study.

### 4.2.3 Results

The exact 15 loading-unloading cycles are simulated. There are 2502 elements and the time for simulation is 480 s. It should be noted that the computational time is almost 4.3 times higher than that of one loading-unloading cycle. The reaction force of the indenter versus the depth of the indentation ball is depicted in Figure 4.11.

From Figure 4.11, the 15 loading-unloading cycles can be clearly observed. The withdrawal of 5 $\mu$m almost retracts the indenter head from contact with the specimen, as shown by the force value of almost 0. Conventionally, these peaks of the F-D curve are subjected to a further calculation to some points on a true stress-true plastic strain curve so that fitting can be realized to find out the constitutive model for the material. However, owing to the new approach with NN, F-D curves are sufficient for model training and prediction, which saves us additional computational time and effort. Figure 4.12 presents the contour maps of the VMS value when the indenter is at the depth of 150 $\mu$m and after its complete withdrawal from the specimen.

Figure 4.12 shows that the maximum von Mises stress when the indenter is at its
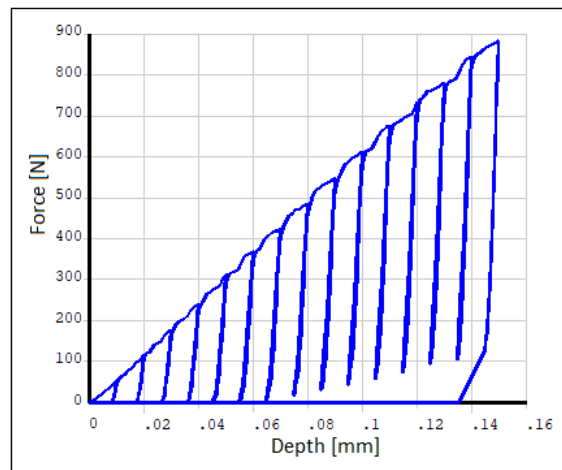
Figure 4.11: F-D curve results for 15 loading-unloading cycles.
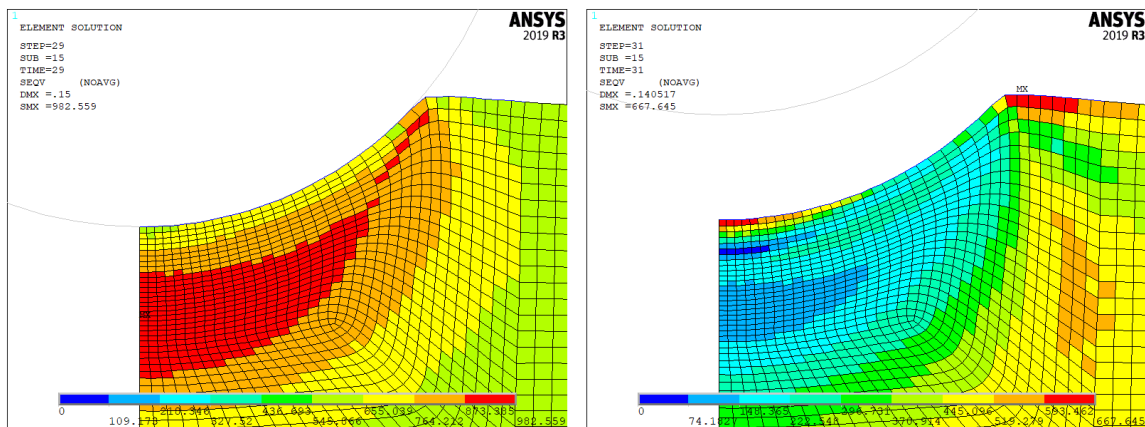


Figure 4.12: VMS results before and after complete withdrawal of the indenter for 15 loading-unloading cycles.

deepest position is 982 MPa (left side), and after it retreats is 667 MPa (right side). The equivalent plastic strain is shown in Figure 4.13.

As can be seen in Figure 4.13, after the withdrawal of the indenter, all the elastic strain is released, left alone the plastic strain. The permanent deformation (imprint of the indenter) is caused by a substantial amount of plastic deformation of the material under the contact surface before the indenter is removed. The maximum equivalent plastic strain is 1.168. A majority of the permanently deformed region is with equivalent plastic strain ranges between 0.19 and 0.91.
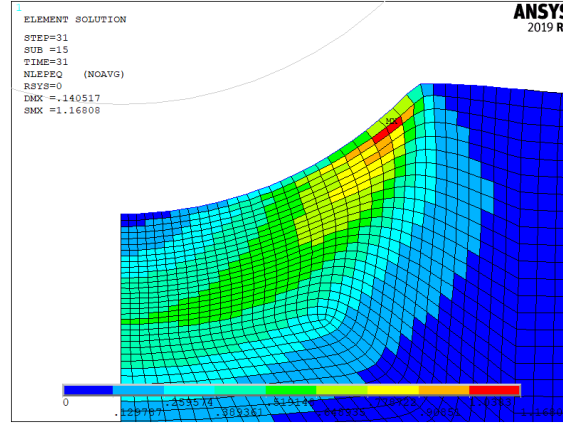
Figure 4.13: Equivalent plastic strain after complete withdrawal of the indenter for 15 loading-unloading cycles.

## 4.3 Model validation

### 4.3.1 Validation of simulated results

The simulation at this stage is ready for the automization process in which the parameters ($\sigma_y$, $C_1$, $\gamma_1$, $C_2$, $\gamma_2$) are varied within specific ranges to input into the FEM model to obtain a corresponding number of F-D curves. These curves are used for the purpose of subsequent NN training. In order to reduce the number of simulations when shuffling the parameter set, the study considers stabilized values of $C_1$ and $\gamma_1$ and adds them to $\sigma_y$. The CHAB5 model utilized so far for the simulation in Equation (4.3) becomes the AF model as follows

$$\sigma = \sigma_y + \frac{C_1}{\gamma_1}(1 - e^{-\gamma_1 \varepsilon_{pl}}). \tag{4.11}$$

It should be noted that in the stabilized state, where the term $\varepsilon_{pl}$ stabilizes at a value less than 1 and is multiplied with usually a very large $\gamma_1$, the product of $-\gamma_1 \varepsilon_{pl}$ will become negatively large. This results in the near 0 product of the term $e^{-\gamma_1 \varepsilon_{pl}}$, thus, making the term $1 - e^{-\gamma_1 \varepsilon_{pl}}$ approximately 1. Therefore, the new $\sigma_y$ in this case is equal to the summation of $\sigma_y$ and $C_1/\gamma_1$ ($=\sigma_\infty$). Using Equation (4.11), the number of parameters is reduced from five to only three ($\sigma_y$, $C_1$, and $\gamma_1$), which is now equivalent to the AF model. The next step is to validate whether this AF model returns the same F-D results as the CHAB5 model that is previously used. The recalculated parameters for the AF model from the CHAB5 model are listed in Table 4.5.

Table 4.5: Conversion of curve fitted material parameters from CHAB model to AF model.

| Model | $\sigma_y$ [MPa] | $C_1$ [MPa] | $\gamma_1$ | $C_2$ [MPa] | $\gamma_2$ |
|-------|------------------|-------------|-----------|-------------|-----------|
| CHAB5 | 330 | 73185 | 357 | 1568 | 2 |
| AF | 535 | 1567 | 2 | 0 | 0 |

In Table 4.5, $\sigma_y$ has been summed up with $C_1/\gamma_1$ in the CHAB5 model to result in the new $\sigma_y$ in AF model. Besides, $C_2$ and $\gamma_2$ in CHAB5 model have become $C_1$ and $\gamma_1$ in AF model. The F-D curves obtained from FEM simulation using CHAB5 and AF material models are plotted in Figure 4.14 and compared with the experiment.
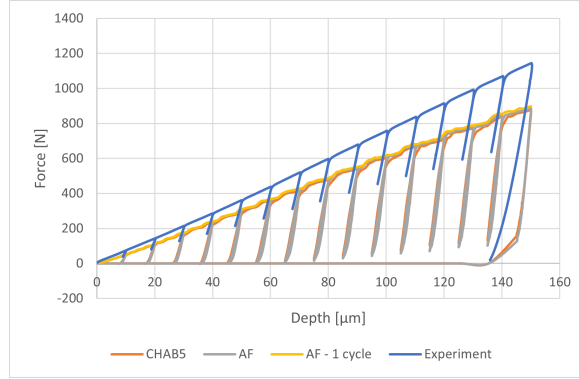


Figure 4.14: F-D results with the use of AF and CHAB5 model in comparison with IIT result.

The F-D curves for the two constitutive models are approximately the same indicating that the AF (with fewer parameters) can be used instead of the CHAB5 model for the simulation. This is better for later working with NN because it reduces significantly the number of training samples. It should be noted as well that there is a need to add a compliance to the F-D results collected from the FEM so that it correlates better with the setup of the machine.

Conventionally, the full information on loading-unloading cycles is important because of the need to consider each peak of force at each cycle to back-calculate a point on the true stress-true plastic strain curve. By taking five peaks of five consecutive loading-unloading cycles in F-D curve, one can calculate, following the procedure described in [1], five true stress-true plastic strain points. From these points, an appropriate material model can be found by curve fitting and the corresponding material parameters can be calculated.

However, herein, the combination of FEM and NN is employed in an attempt to avoid completely the conventional calculating procedure. The new approach is that F-D curves are collected from the FEM instead of IIT. Then, point 0 and the point at which the force is the highest are recorded. From these two points, a line is created and added with a fixed compliance so that it best reflects the physical measurement. By this approach, only the slope of the straight portion of the F-D curve is important and the unloading cycles are neglectable. It is equivalent to having only one loading-unloading cycle which is proven to be feasible as in [71]. This explains why only the depth-controlled approach is used instead of combining force-controlled and depth-controlled approaches in the real scenario, which would considerably complicate the simulation process.

### 4.3.2 Compliance calculation

The simulated result is lower than the experimental result obtained from the IIT measurement due to the compliance of the machine, which can be seen from the difference between the two highest points of the two curves in Figure 4.15.
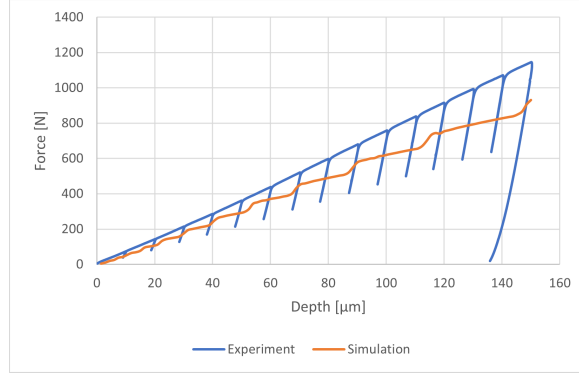


Figure 4.15: Comparison between the experiment (15 cycles), and the simulation (one cycle).

Figure 4.15 shows the maximum force of the experiment is 1145 N while the maximum force of the simulation is 931 N. Thus, the compliance is calculated to be 214 N. This compliance will be added to all the F-D results that will be used for ML model.

### 4.3.3 Creation of dataset with FEM model

The parameters of AF model in Table 4.5 are varied within their ranges (or domains), $\sigma_y \in [175; 400]$ MPa - step size 25 MPa, $\sigma_\infty \in [500; 950]$ MPa - step size 50 MPa, $\gamma_1 \in [1; 10]$ - step size 1. Remarkably, for simulation in APDL, $\sigma_\infty$ has to be recalculated to $C1 \in [500; 9500]$ MPa - step size 500 MPa, for inputs of AF model. As a result, for the combination of 10 values for each parameter $\sigma_y$, $C1$, and $\gamma_1$, it is possible to obtain 1000 different true stress-true plastic strain inputs as shown in Figure 4.16.

Each unique combination of the three parameters is called a configuration. In total, there are 1000 configurations in Figure 4.16 for simulation in APDL. The 1000 maximum force values extracted from the F-D curves before and after adding compliance are shown in Figure 4.17.

The results from Figure 4.17 can be utilized for further training with ML. It should be noted that only the last point (maximum force) of each simulation for NN (only one value) is needed. The force, after being added with a compliance, varies between a range, $F \in [475.502; 1750.89]$ N. The minimum and maximum force have, respectively, the corresponding material parameters $\sigma_y$, $C1$, $\gamma_1$ of 175 MPa, 500 MPa, 10; and 400 MPa, 9500 MPa, 1. It should be noted that, in practice, the F-D curve obtained from the IIT measurement is not a straight line. Therefore, a better approach is to calculate the compliance for all 15 peaks and add those compliance values to every 10 $\mu$m of depth. However, due to the fact that the F-D curve in FEM simulation is simplified to indent 150 $\mu$m in one loading cycle and the model is meshed with a relatively small number of elements, the peaks in between
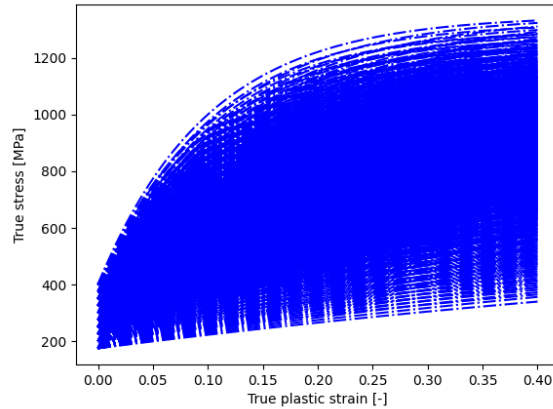
Figure 4.16: True stress-true plastic strain curves from CHAB model using 1000 configurations.
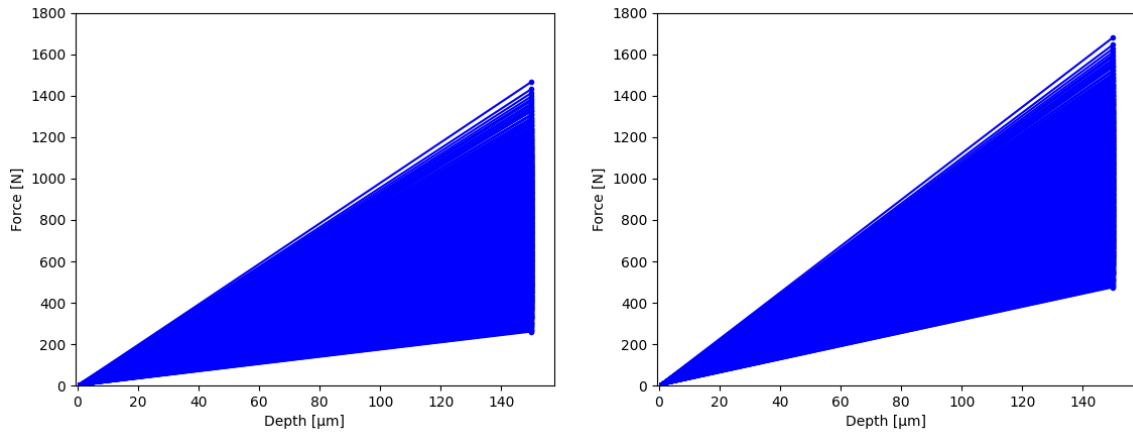


Figure 4.17: F-D curves simulated with 1000 configurations before (left) and after adding the machine compliance (right).

0 $\mu$m and 150 $\mu$m are not with sufficient accuracy to be considered for ML study.

For improvement, 15 cycles should be modeled in FEM simulation. The number of elements should be double or triple the current one. For each peak, a separate compliance value must be added to better calibrate the simulation with reality. Moreover, different constitutive models with different number of parameters can be considered to describe the behaviour of the material more appropriately. These changes should be carried out with caution that the computational time will increase by many folds and more effort is required for pre- and post-processing of the data.

# Chapter 5

# Neural Network

## 5.1 Neural Network setup

### 5.1.1 Neural Network construction

Python language 3.11.0 is utilized for NN construction and visualization of data for the whole study. The primary packages that are employed are numpy 1.23.5, pandas 2.0.0, plotly 5.14.1, sklearn 0.0.post2, tensorflow 2.12.0, matplotlib 3.7.1, etc. The FFNN is implemented with the help of tensorflow package. The network can be constructed with inputs from users regarding how the dataset is divided into training set and testing set, the number of nodes in input/output layers, the number of hidden layers and the number of nodes on each layer, the optimizer (herein Adam), the loss function, the number of epochs, etc.

### 5.1.2 Training and testing data

Each configuration of parameters of CHAB mode can be input into ANSYS APDL and obtain one corresponding F-D curve. By varying the parameters in specific ranges, combining them, and inputting them to ANSYS APDL, one can obtain a set of multiple F-D curves, which can later be used to train and test the NN. The set of samples is divided in this study by 80-20, 80% is used for training while 20% is used for testing the accuracy of the trained model. The aim is to minimize the loss function that indicates the differences between the real values and the prediction. The study first investigates the performance of the proposed NN using a dataset of 1000 samples and later expands it to 7859 samples. Because the parameters and the resulting force are real values with high variation, it is necessary to normalize the data within small ranges such as [-1; 1] and [0; 1]. Small values in uniform format are better for training and testing of NN [72].

### 5.1.3 Training and testing procedure

After having collected a set of 1000 different F-D curves, the force values and their corresponding combinations of three parameters are separated to be the input and output for NN, respectively. The values are normalized and fed into a FFNN. The loss and variation of the predicted parameters from the real parameters are evaluated. The NN is reconstructed as an attempt to minimize the loss. A NN that is successfully trained can take force value(s) from the experiment and return parameters for the constitutive model with high accuracy. This helps to get rid of the burden of calculation using complicated formulas from empirical

studies in the existing literature (many material constants are highly dependent on the material being tested), and the simulation tool (expertise in FEM and professional software) [63].

### 5.1.4 Data preparation

The automatized simulation of IIT with one loading cycle results in 1000 F-D curves. The three parameters and their corresponding force from each simulation are extracted and added to a numpy matrix (.npy). Because these data vary in a wide range with different magnitude, it is necessary to normalize the data so that the NN can calculate the weights and biases easier. In this study, the data is normalized in the range of [0; 1]. To train the NN, there is a need to split the original dataset of the maximum force values and randomized them. In this study, the dataset is split so that 80% is used for training and 20% is used for testing the trained NN. The maximum force values collected from 1000 simulations and 80% of it after splitting and randomization are shown in Figure 5.1.
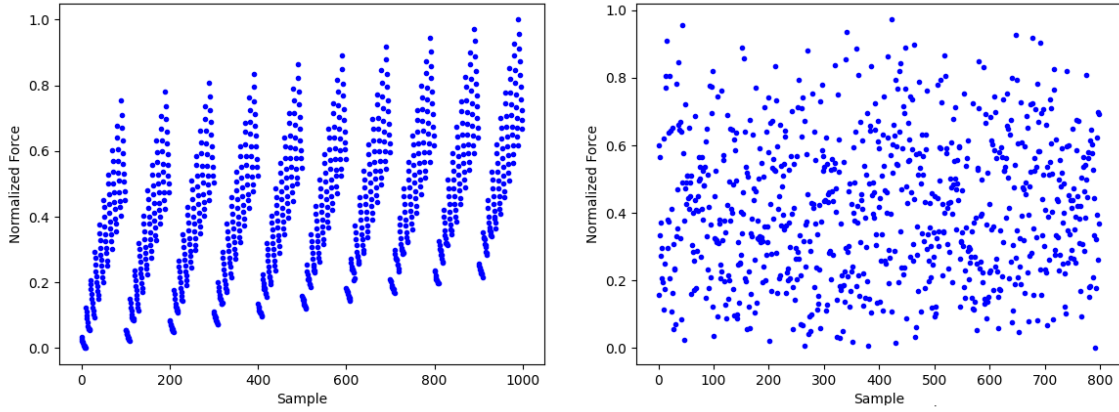


Figure 5.1: The simulated force values: original dataset with 1000 force values (left), and training dataset with 800 force values after splitting and randomization (right).

It can be seen that the original set of force values in Figure 5.1 (left) are relatively structured. This is because the simulations are realized with variation of material parameters in order. After splitting and randomization, the force values for training in Figure 5.1 (right) are almost arbitrarily distributed. This would later complicate the training and testing of the NN because it has to find a function that fits well with the data using the LSM or Mean Square Error (MSE). This is the key parameter for assessing the accuracy of a NN.

As a remark, in the code and graphs shown later in this study, X stands for the input and y for the output. The training data (80%) is with ending _train_ and the prediction based on the training data is with ending _tr_. In the same manner, the testing data (20%) is with ending _test_ and the prediction based on the testing data is with ending _te_.

## 5.2 Results

### 5.2.1 Neural Network structure

We study first the effect of different NN structures on the loss values. The NN is built with one input and three outputs. The sigmoid function is applied for all the nodes. The number of epochs is set to 150 so that saturation is observed. The learning rate is 0.001. The training data is normalized between [0; 1]. The results are shown in Table 5.1.

Table 5.1: Comparison of loss values of different NN structures.

| Hidden layer | 1 | 1 | 3 | 3 | 3 | 5 | 5 | 5 |
|---|---|---|---|---|---|---|---|---|
| Node/hidden layer | 5 | 10 | 1 | 5 | 10 | 1 | 5 | 10 |
| Total hidden nodes | 5 | 10 | 3 | 15 | 30 | 5 | 25 | 50 |
| Loss | 0.0698 | 0.0698 | 0.1026 | 0.0696 | 0.0685 | 0.1025 | 0.0715 | 0.0678 |

It should be noted that the loss results vary slightly given a number of factors: the evaluating procedure, the numerical precision, and the stochastic nature of the algorithm. Therefore, each simulation is run a few times and only the average outcomes are reported. It can be observed in Table 5.1 that the lowest loss that can be obtained is with a NN of ten hidden layers, each with five nodes. The result is, however, comparable with the simplest structure of one hidden layer, each with five nodes. Remarkably, the loss values higher than 0.10 exhibit an interesting pattern. Figure 5.2 illustrates how the training data is predicted by showing the results of the NN with three hidden layers, each with one node.

Analytically, to interpolate such a noisy dataset, one of the best solutions is to calculate the average value, which results in a straight line for the prediction as shown in Figure 5.2. This is undesirable for us because it means that the three parameters remain constant regardless of the force value. The NN with one hidden layer containing five nodes is the most reasonable in terms of the loss value and simplicity of the structure. This NN structure is utilized for further studies and the results are presented in the below subsections.

### 5.2.2 Activation function

The NN structure with one hidden layer containing five nodes is studied in combination with different activation functions. The key performance indicators are the loss versus epoch, and error between the real data (y_test) and the prediction (pred_te). For better visualization, only the first 100 samples are plotted. The activation function remains to be sigmoid. Figure 5.3 shows the results.

As illustrated in Figure 5.3, the sigmoid function convereges slowly to a loss value of 0.0698. The prediction of parameter 1 follows the trend of the training data. Notably, the prediction of parameter 2 fits the best to training data. However, the prediction of parameter 3 has a significant gap in comparison with the training data and the trend is almost opposite.
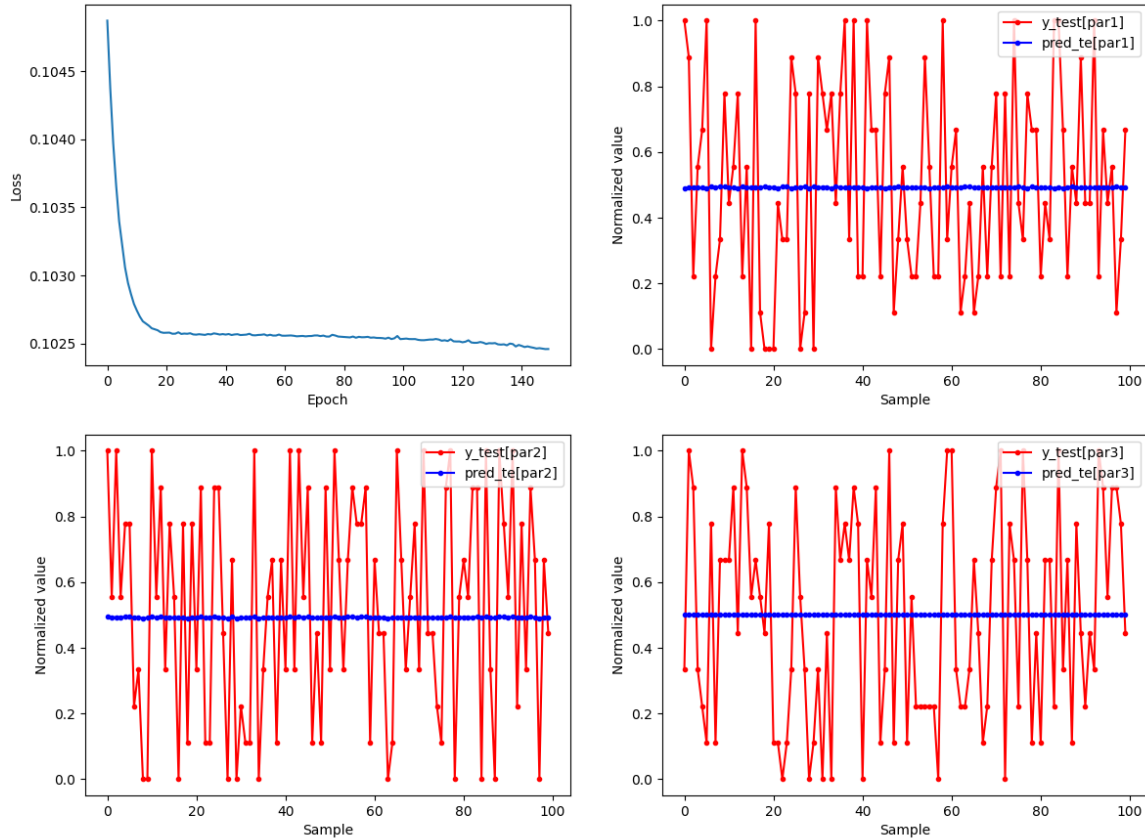
Figure 5.2: Evaluation of NN structure: Loss versus epoch, and error between the real data and the prediction. The almost constant blue lines indicate that the parameters are not learned properly for some NN structures.

Sigmoid function is then changed to softplus function. Using the same structure, the results are shown in Figure 5.4.

The loss in Figure 5.4 is 0.072, which is slightly worse than that of sigmoid. Moreover, for parameter 2, wrong predictions (bigger than 1) are made. It can be drawn that the softplus activation function with the herein NN structure is not appropriate for such a task. Therefore, the sigmoid function is used for further study.

### 5.2.3 Separate evaluation of each parameter

The three parameters are then evaluated separately to observe if the loss value can be better. The NN structure has one input, one hidden layer with five nodes, and one output. The activation function is sigmoid. The results are shown in Figure 5.5, Figure 5.6, and Figure 5.7.

As can be observed in Figure 5.5, Figure 5.6, and Figure 5.7, separated training of parameters 1, 2, and 3 results in respectively the loss of 0.0922, 0.0255, and 0.0965. The
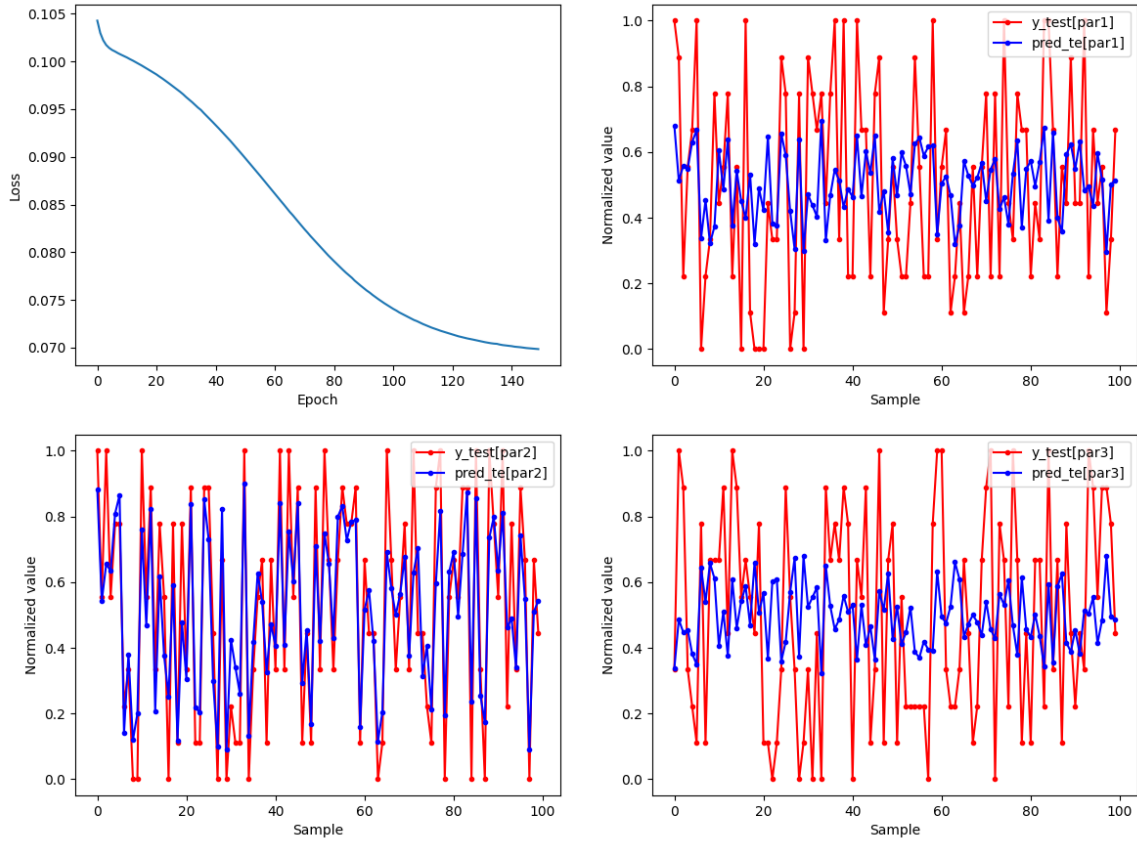
Figure 5.3: Evaluation of NN with sigmoid activation function: Loss versus epoch, and error between the real data and the prediction.

predicted parameter 1 follows the trend of the training data but with a significant difference. The prediction of parameter 2 fits the best to the training data. Meanwhile, the predicted parameter 3 goes in the opposite direction to the training data. In other words, parameter 2 is the best learned but not the others. From the material point of view, parameter 2 corresponds to $C$ in the AF constitutive model, which defines the initial slope of the plastic curve from point $\sigma_y$. Indeed, the yield limit of the material has been exceeded within the very first few loading-unloading cycles, evident from the physical IIT. The material behavior after being indented deeper than this threshold value up to 150 $\mu$m is primarily plastic. Therefore, it is reasonable that parameter 2 has the highest influence on the force value that is predicted.

### 5.2.4 Reversed model

Mathematically, it is better for the NN model to interpolate if there are more inputs than outputs [73]. Therefore, the thesis proceeds with an investigation of a reversed structure of the above NN model with three inputs (three parameters) and one output (one maximum force value). The NN is with one hidden layer consisting of five nodes. The activation
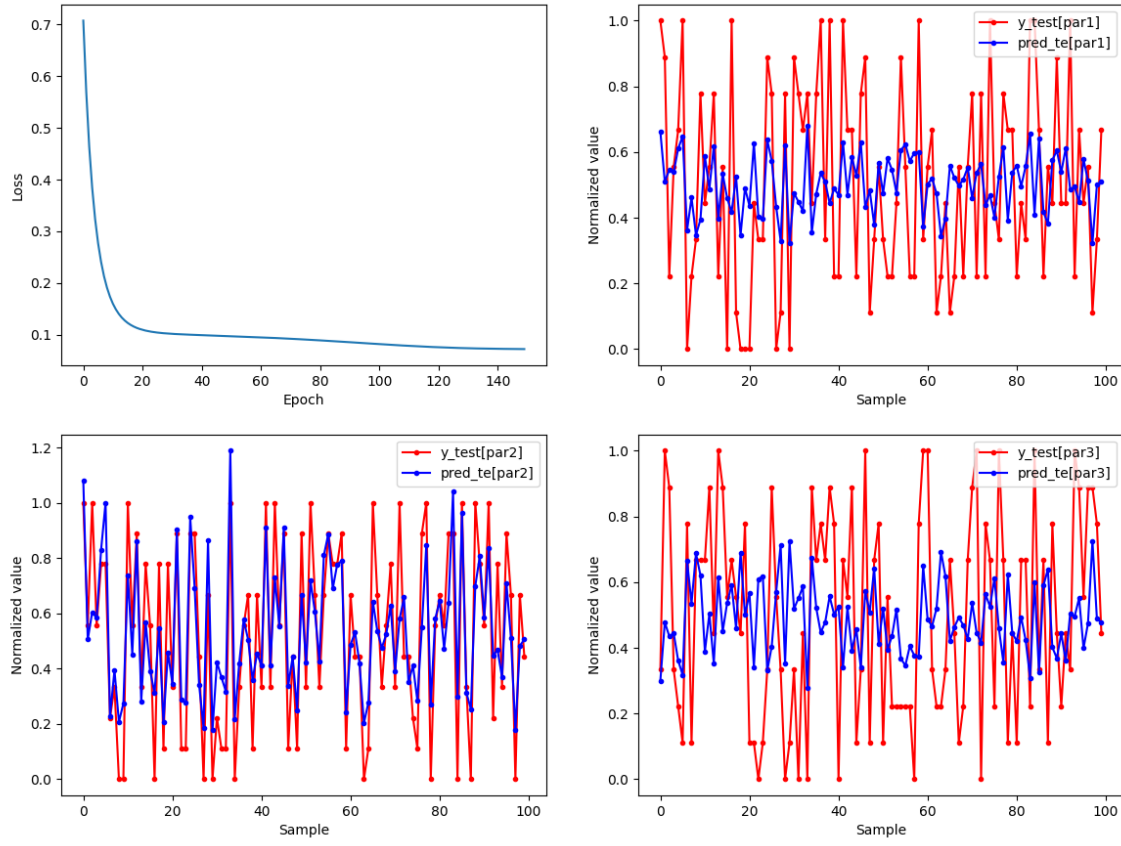
Figure 5.4: Evaluation of NN with softplus activation function: Loss versus epoch, and error between the real data and the prediction.

function is sigmoid. The model with one input and three outputs is henceforward called the original model. The loss value and deviation of the prediction of maximum force from the training value are shown in Figure 5.8.

As shown in Figure 5.8, the loss value is 0.001. It should be noted that, in principle, the fitting functions cannot approximate (or learn) the outliers. This is a common issue in ML applications, in general, the learning model has difficulties learning the extremes, they work much better over smooth and regular functions. In general, the force values are predicted with considerably high accuracy. This confirms the hypothesis that the higher the number of inputs than outputs, the better the prediction with NN model. With this level of accuracy, the reversed NN model can be used to replace the FEM model in APDL with acceptable error.

### 5.2.5 Usage of reversed model

The reversed model predicts well the force values from three inputs. As a result, the reversed model can be employed instead of the FEM simulation in APDL (with acceptable
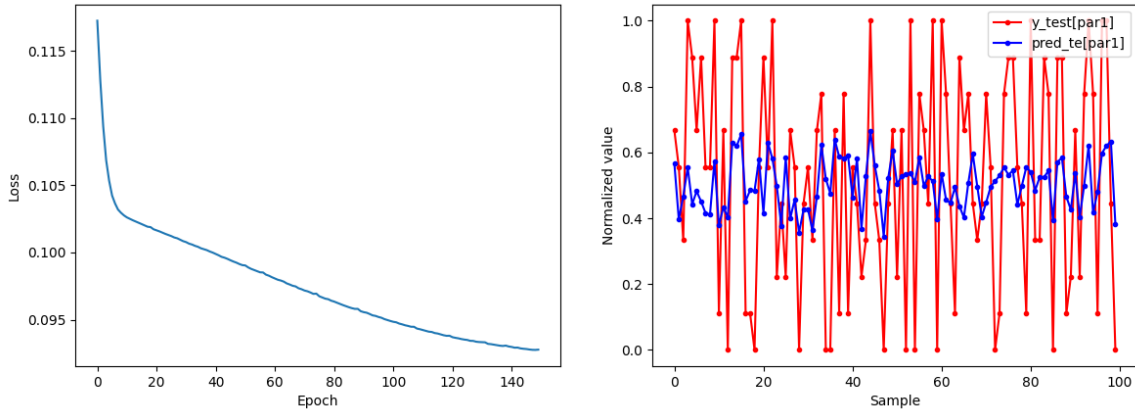
Figure 5.5: Evaluation of NN in predicting only parameter 1: Loss versus epoch, and error between the real data and the prediction.
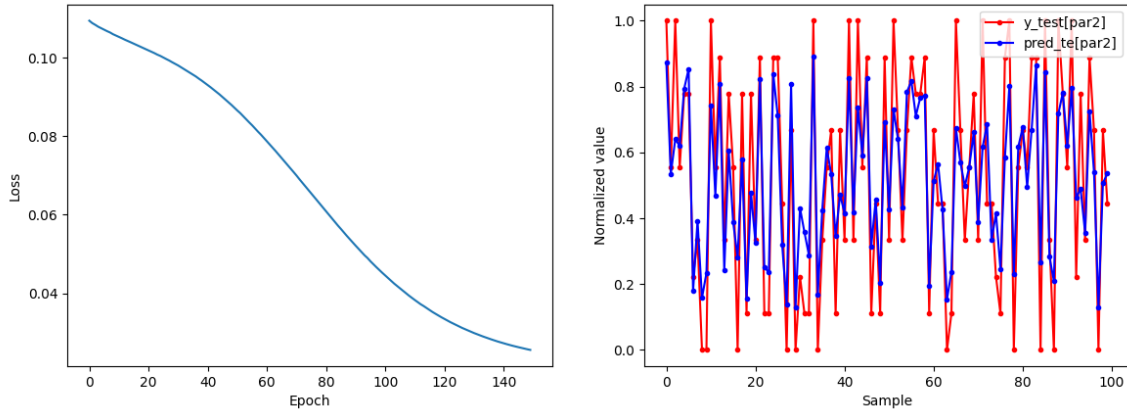


Figure 5.6: Evaluation of NN in predicting only parameter 2: Loss versus epoch, and error between the real data and the prediction.

error) to create more force prediction from a higher number of parameter configurations.

For example, by halving the step size for variation of the three parameters in their domains, the number of configurations can be increased from 1000 to 6859. These 6859 configurations can be input into the reversed model to predict the corresponding 6859 maximum force values. Subsequently, 6859 sets of parameters and corresponding forces (obtained from the reversed model) are collected and combined with the previous 1000 results (obtained from simulation in APDL) to create a larger dataset that can be used to train the original NN model. This is done to increase the number of samples in an attempt to reduce the loss value of the original model.

Because of the increased number of data, the structure of the original model is modified to have three hidden layers, each with 10 nodes. The activation function remains to be sigmoid. The results of training with 7859 samples are shown in Figure 5.9.
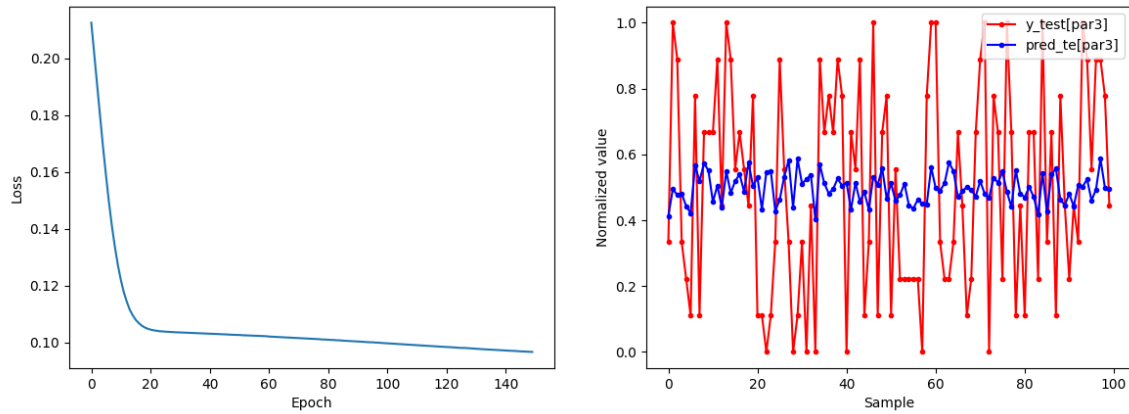
Figure 5.7: Evaluation of NN in predicting only parameter 3: Loss versus epoch, and error between the real data and the prediction.
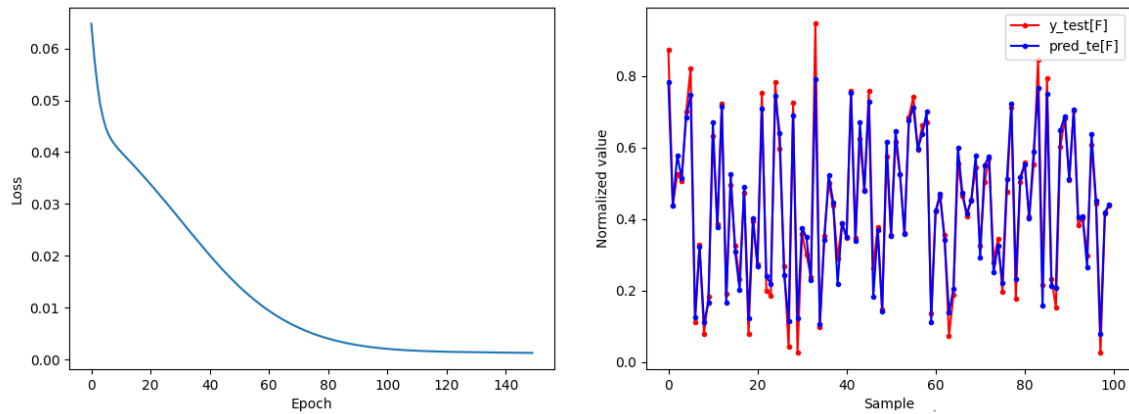


Figure 5.8: Evaluation of the reversed NN in predicting force: Loss versus epoch, and error between the real data and the prediction.

In Figure 5.9, there is a steep drop in loss value within the first 20 epochs. The loss converges then to the value of 0.0610. In comparison with the original model in Figure 5.3, the loss value is almost 1% better. Parameter 2 is still the best prediction. Notably, owing to the increase of input samples, parameter 3 is better approximated, evident from the fact that the prediction starts following the trend line of the train data. This confirms the hypothesis that the higher the number of training samples, the better the prediction of the NN model. In general, there is not a significant improvement in terms of statistical differences.
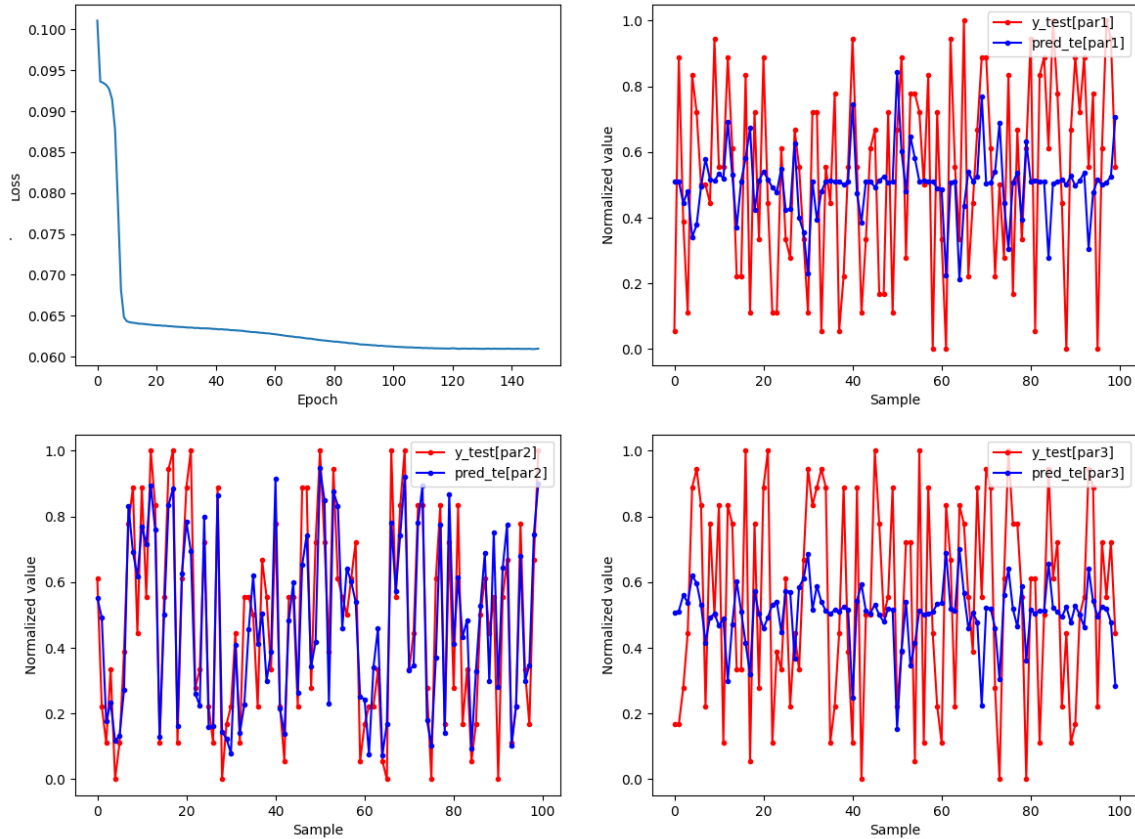
Figure 5.9: Evaluation of NN trained with 7859 samples: Loss versus epoch, and error between the real data and the prediction.

The three parameters are studied separately following the above procedure. The results can be observed in Figure 5.10, Figure 5.11, and Figure 5.12.

Similar to the previous results with 1000-sample training, parameter 2 is best learned. The loss values observed in Figure 5.10, Figure 5.11, and Figure 5.12 for parameters 1, 2, and 3 are respectively 0.0839, 0.0205, and 0.0852. Parameters 1 and 3 are used together to train the NN, which results in a loss value of 0.0845. By increasing the number of training samples to almost eight times, the loss value decreases approximately 1% for parameter 1 and parameter 3. Whether these two parameters are trained separately or together has almost no influence on the accuracy of the NN model. For parameter 2, the loss value is 0.5% indicating that increasing training samples does not have the same effect on all parameters.

Besides, one has to consider the fact that the supplementary 6859 results generated from the reversed NN contain already prediction errors. This would result in substantial accumulated error the more samples are generated and employed. Moreover, it should be noted that FEM is an approximating method by its nature, which inevitably downgrades the performance of the model if it is not calibrated well with the physical measurement.
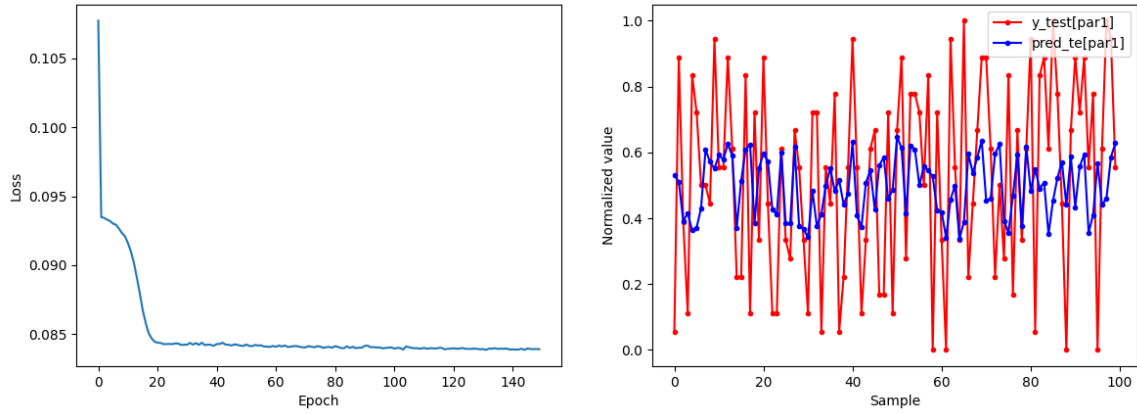
Figure 5.10: Evaluation of NN trained with 7859 samples in predicting only parameter 1: Loss versus epoch, and error between the real data and the prediction.



Figure 5.11: Evaluation of NN trained with 7859 samples in predicting only parameter 2: Loss versus epoch, and error between the real data and the prediction.



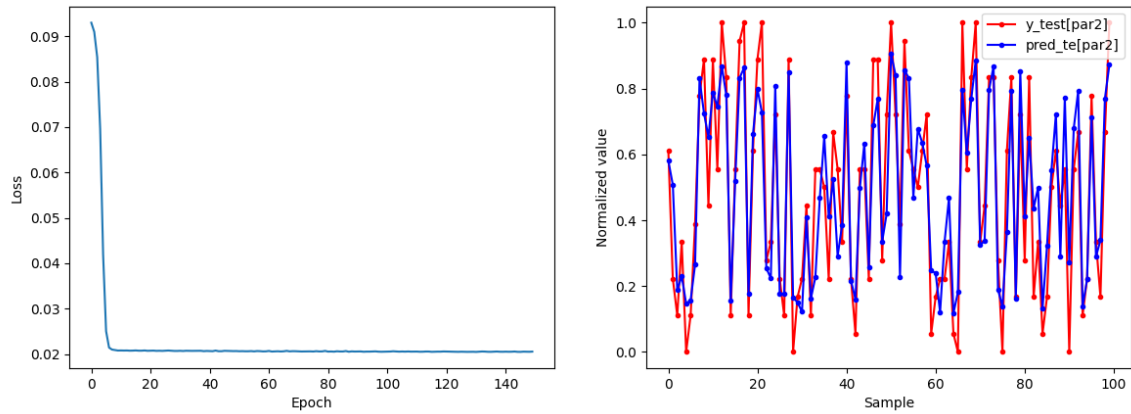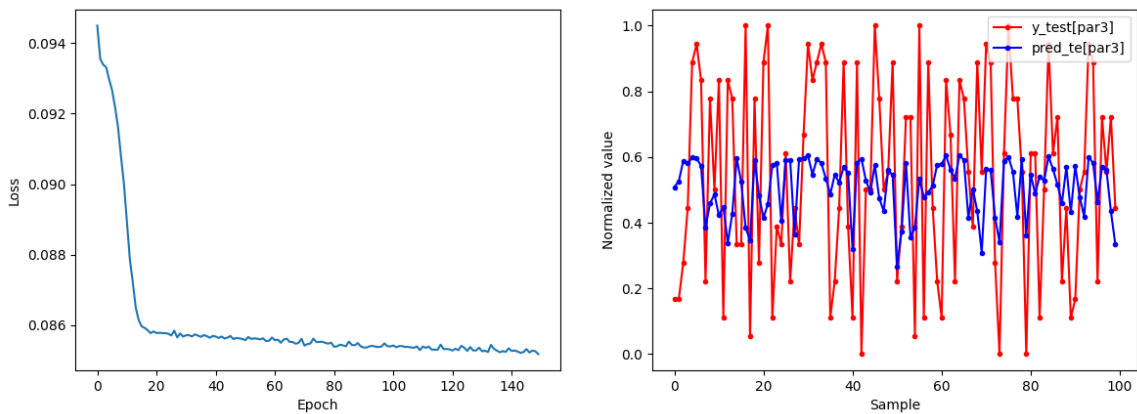Figure 5.12: Evaluation of NN trained with 7859 samples in predicting only parameter 3: Loss versus epoch, and error between the real data and the prediction.

# Chapter 6

# Conclusions and Future work

The final goal of the study has been accomplished, that is, to create a framework that incorporates FEM and NN to evaluate the experimental data from a physical IIT on a material and directly calibrate a suitable plasticity model for it. The study is conducted on austenitic steel SS304L that contains high Chromium composition and therefore is soft by its nature. The material has been a challenge for IIT because the technology requires accurate measurement of the imprint area and corresponding F-D curve to derive the mechanical properties following the stress-strain approach. A solution for this is the application of NNs where the F-D curve is the only input that is needed. A FEM model is then utilized to simulate several IITs and a NN is employed to learn the patterns from the simulated data. Once appropriately trained, this NN can intake an F-D curve and predict the corresponding parameters for the plasticity model of the material with high accuracy.

Specifically, IITs are conducted on a SS304L specimen to obtain a set of F-D curves as references. Then, the tensile test with DIC are carried out on dog-bone specimens machined from the same billet to obtain a set of stress-strain curves. A presentative curve is chosen for fitting with the CHAB model with LSM. The fitted model is later used to describe the plastic behavior of the material under IIT simulation with FEM. The software employed for FEM modelling of IIT is ANSYS APDL. After adding the compliance to the F-D curve obtained for this first simulation, the FEM is calibrated. Then, a variation of the material parameters of the CHAB model is conducted to produce 1000 configurations, from which 1000 corresponding F-D curves can be simulated. It should be noted that these curves should be added with a compliance to reflex reality. From these curves, 1000 maximum forces are extracted and combined with 1000 configurations of material parameters to make an input dataset for training a FFNN. To find the optimal NN model for the task, different structures and different training approaches are investigated. Reported in the thesis is also the use a reversed structure of the NN to increase the number of samples in the input dataset from 1000 samples to 7859 samples. The 7859 samples are subject to the same procedure as the 1000 samples with the NN study. The following paragraphs summarize the contributions of the thesis and its drawbacks, from which directions for future works are discussed.

**Physical test with IIT:** The influence of the surface roughness of the specimen on IIT results is not yet studied. Based on the difference in maximum force (hardness) measured along the diameter, one can acknowledge that the cold-drawn SS304L bar is not an ideal material for the study because it is in-homogeneous. It also suggests that for such a billet, any additional machining that removes the outer layer with higher strength is unfavorable because it leaves only the weak core with lower strength for the final machined parts. On the other hand, it can be drawn that PIIS 3000 machine from the UTM company is able to

measure the local hardness with consistent results. This is evident from the gradual change of the F-D curves from high to low as IIT is conducted from the outer surface toward the core. Another factor that may affect the results is the modelling of loading-unloading cycles, where the loading phase is depth-controlled (indents 10 $\mu$m per step) and the unloading phase is force-controlled (retracts 50 % of force per step). In practice, one can change the setup for indentation and retraction to better suit their needs. For example, one of the possible adjustments is to increase/decrease the indenting depth or fully withdraw the indenter after each step to totally release the elastic strain, leaving alone the plastic strain at the imprint.

**Tensile test with DIC measurement:** Because the material is soft, the close-up view of the fracture shows remarkably clear imprints inherited from the cutting tool. The effect of this phenomenon on the tensile strength of the SS304L specimen is unknown. It is only visible after the specimen has been significantly elongated to failure. Indeed, the machined surface is so smooth that the paint cannot stick well. Besides, the strain-rate dependency of the material can be considered for future FEM simulation.

**FEM simulation in ANSYS APDL:** The thesis prioritizes establishing the workflow, therefore, only one value of machine compliance is employed. In fact, the line that connects the maximum forces over the depth in IIT is nonlinear. In other words, the compliance for each loading-unloading cycle is different. Therefore, it is necessary to simulate 15 loading-unloading cycles and add the corresponding compliance to model better the reality. Moreover, for better accuracy, it is possible to prepare the geometry with finer mesh and increase the number of steps in each cycle of the simulation. The simultaneous force/depth control can be modeled as well. However, one has to consider the fact that each improvement will increase the computational time by many folds and the FEM model will be automated to produce a huge number of F-D results for later NN training. Moreover, different constitutive models to describe strain-hardening and/or time-hardening behaviors can be employed.

**NN training:** The FFNN model learns well parameter 2, which is $C$ in the AF constitutive model. From the material point of view, $C$ defines the initial slope of the plastic curve from point $\sigma_y$. Therefore, it is reasonable that it has the highest influence on the force value that is predicted because the behavior of the material during IIT is almost in the plastic region (permanent deformation). To improve the performance of the NN, it is necessary to experiment with different activation functions or architectures in terms of the number of nodes and hidden layers. Besides, instead of FFNN, different types of NN can be considered. It should be noted that the input force for the approximation task is almost a white noise distribution with many outliers. Therefore, one of the possible improvements would be to smooth the dataset of forces by filtering the outliers using a predefined window so that it becomes less noisy and the approximation by NN can be realized better. Another approach is to increase the number of training data by simulating more configurations. The number of inputs can be increased as well by simulating the full 15 loading-unloading cycles so that for each configuration, there are 15 maximum force values (after each loading-unloading cycle with compliance added) instead of one force value as studied herein. Furthermore, other ML techniques can be analyzed in the future. Besides, it would be good to integrate methods for augmenting the training data (such as Bagging or other strategies for sampling). A NN model has been implemented and proves itself to be a promising tool for the highly accurate evaluation of material properties in combination with IIT.

# References

[1] Yingzhi Li **et al**. "Improvement of predicting mechanical properties from spherical indentation test". **In**: *International Journal of Mechanical Sciences* 117 (1 **october** 2016), **pages** 182–196. ISSN: 0020-7403. DOI: 10.1016/j.ijmecsci.2016.08.019.

[2] Herrman Konrad. *Hardness Testing: Principles and Applications - ASM International.* ASM International, 2010. ISBN: 0-61503-832-9.

[3] J. Kimm **et al**. "Micromechanical characterization of hard phases by means of instrumented indentation and scratch testing". **In**: *Materials Science and Engineering: A* 768 (2019), **page** 138480. ISSN: 0921-5093. DOI: 10.1016/j.msea.2019.138480.

[4] S. Blazewski **and** S. Mikoszewski. *Pomiary twardosci metali.* Wydawnictwa Naukowo-Techniczne, Warszawa, 1981, **page** 13.

[5] "Mechanics of Herbert Pendulum Hardness Tester and its Application". **In**: *Key Engineering Materials* 741 (2017), **pages** 122–127. DOI: 10.4028/www.scientific.net/kem.741.122.

[6] Suzuki R. **et al**. "Hardness Measurement for Metals Using Lightweight Herbert Pendulum Hardness Tester With Cylindrical Indenter". **In**: *Experimental Techniques* 40 (2016), **pages** 795–802. DOI: 10.1007/s40799-016-0080-2.

[7] ASTM International E140-12be1. *Standard Hardness Conversion Tables for Metals Relationship Among Brinell Hardness, Vickers Hardness, Rockwell Hardness, Superficial Hardness, Knoop Hardness, Scleroscope Hardness, and Leeb Hardness.* techreport. West Conshohocken, Pennsylvania: ASTM International, 2013.

[8] Hui Chen **and** Li-Xun Cai. "Theoretical Conversions of Different Hardness and Tensile Strength for Ductile Materials Based on Stress–Strain Curves". **In**: *Metallurgical and Materials Transactions A* 49 (2018), **pages** 1090–1101. DOI: 10.1007/s11661-018-4468-8.

[9] W.C. Oliver **and** G.M. Pharr. "An improved technique for determining hardness and elastic modulus using load and displacement sensing indentation experiments". **In**: *Journal of Materials Research* 7.6 (**june** 1992), **pages** 1564–1583. ISSN: 0884-2914, 2044-5326. DOI: 10.1557/JMR.1992.1564.

[10] Jeremy Thurn, Dylan J. Morris **and** Robert F. Cook. "Depth-sensing indentation at macroscopic dimensions". **In**: *Journal of Materials Research* 17.10 (**october** 2002), **pages** 2679–2690. ISSN: 0884-2914, 2044-5326. DOI: 10.1557/JMR.2002.0388.

[11] X. D. Hou **and** N. M. Jennett. "Defining the limits to long-term nano-indentation creep measurement of viscoelastic materials". **In**: *Polymer Testing* 70 (1 **september** 2018), **pages** 297–309. ISSN: 0142-9418. DOI: 10.1016/j.polymertesting.2018.07.022.

[12] Anja Weidner **and** Horst Biermann. "Review on Strain Localization Phenomena Studied by High-Resolution Digital Image Correlation". **In**: *Advanced Engineering Materials* 23.4 (2021), **page** 2001409. DOI: 10.1002/adem.202001409.

[13]  Cédric Bosch **et al**. *21 - Mechanical Tests in Corrosive Environments and Under Gaseous Hydrogen*. Elsevier, 1 **january** 2019, **pages** 481–505. ISBN: 978-1-78548-309-7. DOI: 10.1016/B978-1-78548-309-7.50021-1.

[14]  K Sharmila Sai Sree **and** Srikanth Koniki. "Applications of Non-Contact Digital Image Correlation Method (DIC) – A Review". **In**: *E3S Web of Conferences* 309 (2021), **page** 01175. ISSN: 2267-1242. DOI: 10.1051/e3sconf/202130901175.

[15]  Ma Quanjin **et al**. "Experimental investigation of the tensile test using digital image correlation (DIC) method". **In**: *Materials Today: Proceedings* 27 (2020), **pages** 757–763. ISSN: 2214-7853. DOI: 10.1016/j.matpr.2019.12.072.

[16]  S. Karen Alavi **et al**. "On the applicability of digital image correlation method in extracting the higher order terms in stress field around blunt notches". **In**: *Theoretical and Applied Fracture Mechanics* 121 (**october** 2022), **page** 103436. ISSN: 01678442. DOI: 10.1016/j.tafmec.2022.103436.

[17]  Kaveh Samadian, Stijn Hertelé **and** Wim De Waele. "Using 3D Digital Image Correlation (3D-DIC) to Measure CTOD in a Semi-Elliptical Surface Crack". **In**: MDPI, august 2018. DOI: 10.3390/ICEM18-05311.

[18]  M. A. Rastak **et al**. *16 - Estimation of residual stresses in polymer-matrix composites using digital image correlation*. Woodhead Publishing Series in Composites Science and Engineering. Woodhead Publishing, 1 **january** 2021, **pages** 455–486. ISBN: 978-0-12-818817-0. DOI: 10.1016/B978-0-12-818817-0.00001-9.

[19]  Nick McCormick **and** Jerry Lord. "Digital Image Correlation". **In**: *Materials Today* 13.12 (2010), **pages** 52–54. ISSN: 1369-7021. DOI: 10.1016/S1369-7021(10)70235-2.

[20]  O.C. Zienkiewicz, R.L. Taylor **and** J.Z. Zhu. *Chapter 1 - The Standard Discrete System and Origins of the Finite Element Method*. Seventh Edition. Oxford: Butterworth-Heinemann, 2013, **pages** 1–20. ISBN: 978-1-85617-633-0. DOI: 10.1016/B978-1-85617-633-0.00001-0.

[21]  Wing Kam Liu, Shaofan Li **and** Harold S. Park. "Eighty Years of the Finite Element Method: Birth, Evolution, and Future". **In**: *Archives of Computational Methods in Engineering* 29 (2022), **pages** 4431–4453. DOI: 10.1007/s11831-022-09740-9.

[22]  Jousef Murad. *The Finite Element Method (FEM) – A Beginner's Guide*. URL: https://www.jousefmurad.com/fem/the-finite-element-method-beginners-guide/.

[23]  Radim Halama **et al**. "Contact defects initiation in railroad wheels – Experience, experiments and modelling". **In**: *Wear* 271.1 (2011), **pages** 174–185. ISSN: 0043-1648. DOI: 10.1016/j.wear.2010.10.053.

[24]  Rostislav Cech, Petr Horyl **and** Pavel Marsalek. "Modelling of Two-Seat Connection to the Frame of Rail Wagon in Terms of Resistance at Impact Test". **In**: 66.2 (2016), **pages** 101–106. DOI: 10.1515/scjme-2016-0024.

[25]  David Rybansky **et al**. "Study of Optimal Cam Design of Dual-Axle Spring-Loaded Camming Device". **In**: *Materials* 14.8 (2021). ISSN: 1996-1944. DOI: 10.3390/ma14081940.

[26]  Petr Horyl **et al**. "Parametric Studies of Total Load-Bearing Capacity of Steel Arch Supports". **In**: *Acta Montanistica Slovaca* 24.3 (2019), **pages** 213–222. ISSN: 1335-1788.

[27]   David Krzikalla **et al**. "Analysis of Torsional Stiffness of the Frame of a Formula Student Vehicle". **In**: *Journal of Applied Mechanical Engineering* 8.1 (2019). DOI: `10.35248/2168-9873.19.8.315`.

[28]   Ferdinand P. Beer **et al**. *Mechanics of Materials (7th edition)*. McGraw Hill, 2014. ISBN: 0073398233.

[29]   Byjus. *Yield strength*. URL: `https://byjus.com/physics/yield-strength/`.

[30]   Richard M. Christensen. *The Theory of Materials Failure*. Oxford University Press, 2016. ISBN: 0198794703.

[31]   Kelly PA. *Lecture Notes: An introduction to Solid Mechanics*. URL: `https://pkel015.connect.amazon.auckland.ac.nz/SolidMechanicsBooks/index.html/`.

[32]   ANSYS training. *Metal plasticity - Lesson 2: Yield surface*. URL: `https://courses.ansys.com/wp-content/uploads/2020/12/Lesson-2-Yield-Surface.pdf/`.

[33]   ANSYS training. *Metal plasticity - Lesson 3: Hardening of plasticity*. URL: `https://courses.ansys.com/wp-content/uploads/2020/12/Lesson-3-Hardening-of-Plasticity.pdf/`.

[34]   C.O. Frederick **and** P.J. Armstrong. "A mathematical representation of the multi-axial Bauschinger effect". **In**: *Materials at High Temperatures* 24.1 (30 **april** 2007), **pages** 1–26. ISSN: 09603409. DOI: `10.3184/096034007X207589`.

[35]   J.L. Chaboche. "Time-independent constitutive theories for cyclic plasticity". **In**: *International Journal of Plasticity* 2.2 (**january** 1986), **pages** 149–188. ISSN: 07496419. DOI: `10.1016/0749-6419(86)90010-0`.

[36]   J.L. Chaboche. "Constitutive equations for cyclic plasticity and cyclic viscoplasticity". **In**: *International Journal of Plasticity* 5.3 (**january** 1989), **pages** 247–302. ISSN: 07496419. DOI: `10.1016/0749-6419(89)90015-6`.

[37]   Giovanni B. Broggiato, Francesca Campana **and** Luca Cortese. "The Chaboche nonlinear kinematic hardening model: calibration methodology and validation". **In**: *Meccanica* 43.2 (**april** 2008), **pages** 115–124. ISSN: 0025-6455, 1572-9648. DOI: `10.1007/s11012-008-9115-9`.

[38]   Radim Halama, Frantisek Fojtik **and** Aleksandros Markopoulos. *Memorization and Other Transient Effects of ST52 Steel and Its FE Description*. 2013. DOI: `10.4028/www.scientific.net/amm.486.48`.

[39]   Radim Halama, Josef Sedlak **and** Michal Sofer. *Phenomenological Modelling of Cyclic Plasticity*. InTech, 23 **march** 2012. ISBN: 978-953-51-0219-9. DOI: `10.5772/35902`.

[40]   Åke Björck. "Least squares methods". **In**: *Handbook of Numerical Analysis* 1 (1990), **pages** 465–652. ISSN: 1570-8659. DOI: `10.1016/S1570-8659(05)80036-5`.

[41]   T.J. Hastie **and** R.J. Tibshirani. *Generalized Additive Models*. Generalized Additive Models, 1990. ISBN: 9780412343902.

[42]   Otto M. Heeres, Akke S.J. Suiker **and** René de Borst. "A comparison between the Perzyna viscoplastic model and the Consistency viscoplastic model". **In**: *European Journal of Mechanics - A/Solids* 21.1 (2002), **pages** 1–12. ISSN: 0997-7538. DOI: `10.1016/S0997-7538(01)01188-3`.

[43] Arthur L. Samuel. "Some studies in machine learning using the game of checkers". In: *IBM Journal of Research and Development* 3.3 (**july** 1959), **pages** 210–229. DOI: 10.1147/rd.33.0210.

[44] Pramila P. Shinde **and** Seema Shah. "A Review of Machine Learning and Deep Learning Applications". In: *2018 Fourth International Conference on Computing Communication Control and Automation (ICCUBEA)*. 2018 Fourth International Conference on Computing Communication Control and Automation (ICCUBEA). Pune, India: IEEE, **august** 2018, **pages** 1–6. ISBN: 978-1-5386-5257-2. DOI: 10.1109/ICCUBEA.2018.8697857.

[45] Sebastián Basterrech **and** Gerardo Rubino. "Random Neural Network as Supervised Learning Tool". In: *Neural Network World* (2015). Preprint, estimated publication date: 2016.

[46] T. Hastie, R. Tibshirani **and** J. Friedman. *The elements of Statistical Learning.* Spring series in statistics. New York, USA: Springer-Verlag, 2001. ISBN: 0387952845.

[47] Sebastián Basterrech **et al**. "Levenberg-Marquardt Training Algorithms for Random Neural Networks". In: *Computer Journal* 54 (2011), **pages** 125–135. ISSN: 0010-4620. DOI: 10.1093/comjnl/bxp101.

[48] Isha Salian. *SuperVize Me: What's the Difference Between Supervised, Unsupervised, Semi-Supervised and Reinforcement Learning?* URL: https://blogs.nvidia.com/blog/2018/08/02/supervised-unsupervised-learning/.

[49] Warren S. McCulloch **and** Walter Pitts. "A logical calculus of the ideas immanent in nervous activity". In: *The bulletin of mathematical biophysics* 5.4 (1 **december** 1943), **pages** 115–133. ISSN: 1522-9602. DOI: 10.1007/BF02478259.

[50] Oludare Isaac Abiodun **et al**. "State-of-the-art in artificial neural network applications: A survey". In: *Heliyon* 4.11 (**november** 2018). ISSN: 24058440. DOI: 10.1016/j.heliyon.2018.e00938.

[51] Osval Antonio Montesinos López, Abelardo Montesinos López **and** Jose Crossa. *Fundamentals of Artificial Neural Networks and Deep Learning.* Cham: Springer International Publishing, 2022, **pages** 379–425. ISBN: 978-3-030-89010-0. DOI: https://doi.org/10.1007/978-3-030-89010-0_10.

[52] N. S. Johnson **et al**. *Machine Learning for Materials Developments in Metals Additive Manufacturing.* 2020. arXiv: 2005.05235 [physics.app-ph].

[53] Joshua F. Wiley. *R Deep Learning Essentials: Build Automatic Classification and Prediction Models Using Unsupervised Learning.* Birmingham, United Kingdom: Packt Publishing, 2016. ISBN: 1785280589, 9781785280580.

[54] Dugas Charles **et al**. "Incorporating Second-Order Functional Knowledge for Better Option Pricing". In: *Advances in Neural Information Processing Systems*. **volume** 13. MIT Press, 2000.

[55] Zahraa E. Mohamed. "Using the artificial neural networks for prediction and validating solar radiation". In: *Journal of the Egyptian Mathematical Society* 27.1 (**december** 2019), **page** 47. ISSN: 2090-9128. DOI: 10.1186/s42787-019-0043-8.

[56]  John A.Hertz. *Introduction To The Theory Of Neural Computation*. CRC Press, Boca Raton: Taylor & Francis Group, 2019. ISBN: 978-0-429-49966-1. DOI: https://doi.org/10.1201/9780429499661.

[57]  Francois Chollet **and** J. J. Allaire. *Deep Learning with R*. Manning, 2018. ISBN: 978-1-617-29554-6.

[58]  Josh Patterson **and** Adam Gibson. *Deep Learning: A Practitioner's Approach*. O'Reilly Media, 2017. ISBN: 1491914254.

[59]  Saulo Barreto. *Differences Between Backpropagation and Feedforward Networks*. URL: https://www.baeldung.com/cs/neural-networks-backprop-vs-feedforward/.

[60]  Keras. *Optimizer: Adam*. URL: https://keras.io/api/optimizers/adam/.

[61]  Diederik P. Kingma **and** Jimmy Ba. *Adam: A Method for Stochastic Optimization*. 2017. DOI: 10.48550/arXiv.1412.6980.

[62]  Feng Yu **et al**. "A new instrumented spherical indentation test methodology to determine fracture toughness of high strength steels". **In**: *Theoretical and Applied Fracture Mechanics* 124 (2023), **page** 103744. ISSN: 0167-8442. DOI: 10.1016/j.tafmec.2022.103744.

[63]  Lu Lu **et al**. "Extraction of mechanical properties of materials through deep learning from instrumented indentation". **In**: *Proceedings of the National Academy of Sciences* 117.13 (2020), **pages** 7052–7062. DOI: 10.1073/pnas.1922210117.

[64]  Kyeongjae Jeong **et al**. "Prediction of uniaxial tensile flow using finite element-based indentation and optimized artificial neural networks". **In**: *Materials & Design* 196 (2020), **page** 109104. ISSN: 0264-1275. DOI: 10.1016/j.matdes.2020.109104.

[65]  Hyuk Lee **et al**. "An Investigation of Nanomechanical Properties of Materials using Nanoindentation and Artificial Neural Network". **In**: *Scientific Reports* 9 (2019), **page** 13189. DOI: 10.1038/s41598-019-49780-z.

[66]  S. Salmani Ghanbari **and** A.H. Mahmoudi. "An improvement in data interpretation to estimate residual stresses and mechanical properties using instrumented indentation: A comparison between machine learning and Kriging model". **In**: *Engineering Applications of Artificial Intelligence* 114 (2022), **page** 105186. ISSN: 0952-1976. DOI: 10.1016/j.engappai.2022.105186.

[67]  ISO6506-1:2014. *Metallic materials — Brinell hardness test — Part 1: Test method*. techreport. International Organization for Standardization, 2014.

[68]  UTM-Unconventional testing machine. *PIIS 3000, Non-destructive, portable Instrumented Indentation Tester*. URL: https://utmdev.eu/product/piis3000/non-destructive-portable-instrumented-indentation-tester/.

[69]  Ansyshelp. *Controls Used for Free and Mapped Meshing*. URL: https://ansyshelp.ansys.com/.

[70]  K L Johnson. "One Hundred Years of Hertz Contact". **In**: *Proceedings of the Institution of Mechanical Engineers* 196.1 (1982), **pages** 363–378. DOI: 10.1243/PIME\_PROC\_1982\_196\_039\_02.

[71] A.H. Mahmoudi **and** S.H. Nourbakhsh. "A Neural Networks approach to characterize material properties using the spherical indentation test". **In**: *Procedia Engineering* 10 (2011). 11th International Conference on the Mechanical Behavior of Materials (ICM11), **pages** 3062–3067. ISSN: 1877-7058. DOI: 10.1016/j.proeng.2011.04.507.

[72] J. Sola **and** J. Sevilla. "Importance of input data normalization for the application of neural networks to complex industrial problems". **In**: *IEEE Transactions on Nuclear Science* 44.3 (1997), **pages** 1464–1468. DOI: 10.1109/23.589532.

[73] T. Hegazy, P. Fazio **and** O. Moselhi. "Developing Practical Neural Network Applications Using Back-Propagation". **In**: *Computer-Aided Civil and Infrastructure Engineering* 9.2 (1994), **pages** 145–159. DOI: 10.1111/j.1467-8667.1994.tb00369.x.